
Article:
Meza, F.J., Becque, J. and Hajirasouliha, I. orcid.org/0000-0003-2597-8200 (2020) Experimental study of cold-formed steel built-up columns. Thin-Walled Structures, 149. 106291. ISSN 0263-8231

https://doi.org/10.1016/j.tws.2019.106291

EXPERIMENTAL STUDY OF COLD-FORMED STEEL BUILT-UP COLUMNS

Francisco J. Meza [a], Jurgen Becque [a] and Iman Hajirasouliha [a]

[a] Department of Civil and Structural Engineering, The University of Sheffield, Sheffield, UK

Abstract: A comprehensive experimental programme was contrived with the aim of investigating the behaviour and the capacity of cold-formed steel built-up columns with particular emphasis on the effects of connector spacing and contact between individual components. A total of 24 built-up columns, including four different cross-sectional geometries, were tested between pin-ended boundary conditions, while applying the load with nominal eccentricities of *L*/1000 or *L*/1500. The columns were designed to fail by interaction of cross-sectional buckling of the components, possible global-type buckling of the components between connectors and global buckling of the whole column, and all these failure modes were successfully achieved. The built-up sections were fabricated from flat plates, plain channels and lipped channels and were assembled with either bolts or self-drilling screws. The connector spacing was varied between specimens of the same cross-sectional geometry. Tensile coupons were taken from the flat portions and the corners of the sections in order to determine their material properties, while detailed measurements of the geometric imperfections of each specimen were also carried out using a specially designed measuring rig. In addition, the isolated behaviour of both the bolts and the screws used in the specimens was investigated through single lap shear tests. It was observed that the buckling patterns in the built-up specimens were affected by contact between the various components and by the spacing between the connectors. However, in the cases where global buckling of the components in between connector points was not critical, the connector spacing had a minor influence on the ultimate capacity of the columns.

Keywords: Built-up column; Experiment; Cold-formed steel; Stability; Buckling; Imperfection measurements.

1. Introduction

Cold-formed steel (CFS) built-up sections, assembled by bolting or screwing individual members together, offer practical solutions in light-gauge steel construction in cases where a single section is not able to meet the requirements of load carrying capacity or serviceability. Using the currently available single shapes a wide range of custom-tailored cross-sectional shapes can be obtained. In particular, doubly symmetric cross-sections can easily be constructed, eliminating the shift of the effective centroid resulting from local or distortional buckling, and closed sections can be obtained with increased torsional resistance. Since built-up sections can, in principle, be assembled on site, the advantages associated with single sections, such as ease of transportation, handling and stacking, largely remain.

However, our fundamental understanding of the behaviour of built-up CFS structural members is still rather limited. This can in part be attributed to the fact that the study of their stability issues is an exceedingly challenging task. In addition to the cross-sectional (local and distortional) and global modes of buckling commonly encountered in CFS members, buckling of individual components of the built-up member in between connector points can also occur, while interaction between several or all types of buckling often takes place. As its most important contribution, this paper aims to experimentally study the stability of CFS built-up members and the cross-sectional geometries, lengths and connector spacings of the test specimens were tailored to achieve an array of buckling types and interactions. Second, the experiments sought to specifically quantify the effects of the connector spacing on the ultimate capacity and on the different buckling interactions. This was achieved by varying the connector spacing among otherwise identical specimens. Third, the tests allowed to evaluate the behaviour of the components within the built-up cross-section with reference to that of the isolated component and assess the amount of composite action achieved through contact and interconnections. Both bolts and self-drilling screws were considered as a means to connect the components in order to make data available for both cases. Both types of connectors are commonly used in practice, while they result in a substantially different connection behaviour when subjected to shear. Finally, the paper presents detailed imperfection measurements conducted on the test specimens using a specially designed rig. This alleviates the exceptional scarcity of imperfection data for built-up CFS members.

The programme is the extension of previous research on the cross-sectional capacity of built-up columns, which was carried out by means of 20 stub column tests on similar geometries and is described in detail in

(Meza et al., 2015; Meza et al. 2019). Taking a longer-term view, this paper aims to contribute to the eventual goal of developing practical design guidelines for built-up CFS members through an increased understanding of the phenomena at hand.

2. Literature review

Despite the benefit CFS built-up members can offer, currently the major design codes for CFS (CEN, 2006; AISI, 2016) provide at best only limited provisions in this area, which are only applicable to certain specific types of built-up sections. EN 1993-1-3 (CEN, 2006) does not provide any specific design rules for CFS built-up members, apart from specifying the global buckling curve which should be used to determine the buckling resistance of members with a limited number of open and closed cross-sectional geometries. No guidance is provided on the maximum connector spacing, or on how the connector spacing or the type of connector may affect the ultimate capacity of the member. In addition, there is no consideration of how the individual components may interact with each other when buckling or how this interaction affects the buckling response of the built-up member. The provisions included in the North American Specification (NAS) for the Design of Cold-Formed Steel Structural Members (AISI, 2016) for built-up members in compression apply only to members comprised of two sections in direct contact. The NAS rules require that if global buckling of the built-up column introduces shear forces in the connectors between the components, the slenderness ratio KL/r, which is used in the calculation of the elastic global buckling stress, should be replaced by a modified slenderness ratio. This ratio accounts for the reduced shear rigidity of built-up members connected at discrete points and applies to columns failing by flexural or flexural-torsional buckling. In addition, the NAS (AISI, 2016) provisions limit the connector spacing in order to prevent failure of the individual components due to flexural buckling between connectors in the case that any of the connectors becomes loose or ineffective. Furthermore, the individual components should be connected at the ends of the built-up member by a longitudinal weld having a length of at least the maximum width of the member, or by a dense group of end connectors. The latter should be spaced longitudinally at less than 4 times the diameter of the connectors over a distance of at least 1.5 times the maximum width of the member.

It is worth noting that the modified slenderness formula included in the AISI (2016) provisions was verified against data pertaining to hot-rolled built-up members (Zandonini 1985) and therefore does not necessarily reflect the behaviour of thin-walled CFS members, in which cross-sectional instabilities often occur before

81 global buckling takes place, and in which the geometric imperfections and residual stresses can differ
82 substantially from those encountered in hot-rolled members. In fact, several researchers have questioned the
83 applicability of the modified slenderness approach to thin-walled CFS built-up columns, based on the
84 evidence obtained from experiments (Stone and LaBoube, 2005; Whittle and Ramseyer, 2009; Reyes and
85 Guzmán, 2011).

86 Recently a substantial amount of research has been directed towards extending the applicability of the Direct
87 Strength Method (DSM) to the design of built-up CFS members. Young and Chen (2008) tested built-up
88 columns assembled from channels with intermediate web stiffeners, connected through their flanges using
89 self-tapping screws. The authors showed that the ultimate capacities of the columns were intermediate
90 between the predictions given by the DSM when considering the built-up cross-section as fully integral and
91 the predictions assuming two independent profiles, suggesting that some level of composite action was
92 present. Georgieva et al. (2011, 2012a, 2012b, 2012c) carried out an extensive experimental and numerical
93 investigation to study the buckling behaviour of double-Z built-up columns and assess the accuracy of the
94 DSM predictions. The application of the DSM, based on finite element models to obtain the elastic global
95 buckling stresses, was found to give conservative strength predictions. Zhang and Young (2012) also
96 evaluated the suitability of the DSM to predict the ultimate capacity of built-up I-shaped compression
97 members. The study showed that good agreement between the DSM predictions and the experimental results
98 was achieved when contact between the channels was accounted for by assuming that the thickness of the
99 channel webs in contact with each other was equal to 1.2 times the thickness of the individual channels. More
100 recently, the researchers carried out further studies on closed built-up sections, but concluded that the above
101 approach led to slightly unsafe capacity predictions in those cases (Zhang and Young 2018). An alternative
102 approach was explored in (Zhang and Young, 2015) where the cross-sectional stability analysis of the
103 individual components was carried out with the connectors replaced by longitudinal stiffeners. An
104 experimental investigation of the structural response of CFS I-shaped built-up columns constructed from
105 screw-connected back-to-back lipped channels was reported in (Lu et al., 2017). The authors concluded that
106 there was clear evidence of ultimate strength erosion due to local-distortional and local-distortional-global
107 interaction, and they subsequently proposed a novel direct strength based method to account for these
108 interactions. In addition, they showed that the effect of composite action could be disregarded when failure
109 was predominantly due to local or distortional buckling. Fratamico et al. (2018) also conducted an

experimental investigation of the behaviour and capacity of screw-connected back-to-back lipped channels. However, in this study the columns were seated in tracks, which provided semi-rigid support conditions, typical of those encountered in stud walls. The authors assessed the effect of adding a group of connectors at each end of the column, as prescribed by (AISI, 2016), and confirmed the importance of these end group fasteners (EGFs) in reducing the relative slip between the individual components and increasing the amount of composite action when flexural buckling takes place. Based on the experimental results, an extension to the DSM was proposed, in which the end support conditions were assumed to be fixed and the elastic buckling stresses were calculated using the FSM while modelling the connectors using the smeared constraint approach.

It is worth pointing out that the majority of previous research studies on CFS built-up compression members have focused on geometries fabricated from two identical components, where both components buckled at the same time. In contrast, the experimental programme described in this paper consisted of 24 tests on built-up columns with four different cross-sectional geometries, each of them assembled from two pairs of components with different cross-sections.

3. Section geometry

The four built-up cross-sectional geometries included in the experimental programme are shown in Figure 1. The specimens were designed to fail by interaction between cross-sectional instability, possible global-type buckling of individual components between connectors (depending on the connector spacing) and global flexural buckling of the whole column. For a detailed explanation of the design philosophy which was employed to achieve this, the reader is referred to (Meza, 2018). For each built-up geometry specimens with three different connector spacings were fabricated. Built-up columns 1 and 2 were assembled using grade 8.8 M6 bolts, while built-up columns 3 and 4 were assembled with M5.5 self-drilling screws. Two identical columns were fabricated for each cross-sectional geometry and connector spacing. However, they were tested with slightly different load eccentricities: one specimen had the load applied with an eccentricity of $L/1500$, while its twin specimen was subjected to a slightly larger eccentricity of $L/1000$. All specimens were tested between hinges which only allowed rotation about the major axis of the built-up cross-section. This ensured that the connectors were subject to shear as a result of global flexural buckling of the built-up column.

137 The cross-sectional components were labelled using the letters '*T*', '*S*' or '*P*' to indicate whether they
138 corresponded to a plain channel, a lipped channel or a flat plate component, respectively, followed by the
139 nominal width of the web in mm (in the case of a channel) or the nominal width of the plate in mm, and the
140 nominal wall thickness in mm multiplied by 10. The labelling used to refer to each built-up specimen
141 consisted of the letters '*LC*', followed by a number ranging from 1 to 4 to indicate its cross-sectional geometry
142 (with reference to Figure 1), a hyphen and the number of intermediate rows of connectors (i.e. not counting
143 the connectors in the end sections). Finally, the letters '*a*' and '*b*' were used to differentiate between the tests
144 with eccentricities of *L*/1000 and *L*/1500, respectively. As an example, the label '*LC*1-2*a*' refers to the column
145 with cross-sectional geometry 1 and two intermediate rows of connectors, tested with an eccentricity of
146 *L*/1000.

147 The nominal cross-sectional dimensions of the components used to assemble each built-up geometry fell
148 within the range of geometries allowed by EN 1993-1-3 (CEN, 2006), in particular with respect to their width-
149 to-thickness ratios, and they are listed in Table 1. The relevant symbols are clarified in Figure 2. All columns
150 had a nominal length of 3 m, except columns LC2-2 and LC2-6, which had a length of 2.5 m and columns
151 LC2-4, which were 1.8 m long. These lengths ensured that in all the columns global flexural buckling of the
152 built-up member took place after cross-sectional buckling of the components, while for columns LC2 the two
153 different lengths were chosen in order to include specimens with similar connector spacing but different levels
154 of interaction between global and cross-sectional buckling. All components were fabricated using a brake-
155 pressing procedure by an external specialized fabricator.

156 Prior to assembling the built-up columns the actual cross-sectional dimensions of each component were
157 measured at three different locations along its length. Tables 2-5 list the average cross-sectional dimensions of
158 the components belonging to geometries 1-4, respectively, using the nomenclature established in Figure 2.
159 These values were obtained after deducting the thickness of the zinc coating from the measured dimensions.

160 During the assembly process small diameter holes were first drilled in one component of each pair to be
161 connected at the locations of the connectors. The components were then positioned in their built-up
162 configuration, secured with clamps and spot welded together at each end. Four spot welds were used at each
163 end for each contact pair. The spot welds were designed to ensure a uniform distribution of the stresses over
164 the different components of the built-up specimens upon loading. Finally, bolt holes with a diameter of 6.25

mm were drilled into the specimens with geometries 1 and 2, and the components were bolted together while applying a torque of 10 Nm. This value was deemed representative of manually tightening the bolts with a wrench. The specimens with geometries 3 and 4 were screwed together using self-drilling screws. The locations of the connectors, as well as the arrangement of the spot welds, are illustrated in Figure 3 for all geometries.

Endplates were welded to each end of the columns, after positioning them with the help of lines scribed on both the endplates and the channel webs to indicate their geometric centre lines. The endplates had slotted holes near each corner which allowed for around 10 mm of adjustment when bolting the endplates to the pin supports (Figure 4).

It is worth mentioning that the process of welding on the endplates did not cause any noticeable geometric distortion in the specimens with geometries 3 and 4. However, in the specimens with geometries 1 and 2 some localized distortion was observed near the ends. More specifically, in the specimens with geometry 1 the flat plate components displayed a small out-of-plane bending deformation immediately after welding on the endplates. This deformation was mainly noticeable in the specimens with 2 or 3 intermediate connectors and mostly disappeared after the welded area had cooled down. In the case of the specimens with geometry 2, the flange tips of the T15414 channels moved outwards at each column end after welding on the endplates and although this effect diminished when the welded area cooled down, it was still noticeable in the final state. The flange distortion was most pronounced in specimens LC2-4, as illustrated in Figure 4. It can be expected that these distortions were also accompanied by residual stresses resulting from the heating and cooling process.

4. Material Properties

A total of 26 tensile coupons were tested in order to quantify the material properties of all components of the test specimens. For each type of channel section two flat coupons were taken along the centre line of the web and two corner coupons were cut from the web-flange junction, while for the flat plate components two flat coupons were cut along the centre line of the plate. All flat coupons had a nominal width of 12.5 mm, while the corner coupons had a nominal width of 6 mm. The gauge length was 50 mm in all cases. All coupons were tested following the specifications given in EN ISO 6892-1 (CEN, 2009). The tests were carried out in a 300

192 kN Shimadzu AGS-X universal testing machine and a displacement rate of 1 mm/min was imposed. Each test
193 was halted for 2 minutes at regular intervals in order to eliminate strain rate effects and determine the '*static*'
194 material properties of the coupons (Huang and Young 2014). The (static) engineering values of the material
195 properties are reported in Table 6 as average values for each pair of corresponding coupons. The stress $\sigma_{0.2\%}$
196 corresponds to the 0.2% proof stress and for both the flat and corner coupons was computed based on the
197 Young's modulus obtained from the flat coupons, σ_u is the ultimate tensile strength and ε_f is the elongation
198 after fracture measured over a gauge length of 50 mm. The stress-strain curves of all the tested coupons can be
199 found in (Meza, 2018), which also provides more specifics on the testing arrangement used for the corner
200 coupons, as well as on the novel technique used to measure their cross-sectional area. It is worth mentioning
201 that in the pair of corner coupons extracted from sections T15414(l) failure occurred right next to one of the
202 grips of the extensometer, with a large portion of the localized plastic deformation falling outside the
203 measured gauge length. Therefore, the elongation after fracture obtained for these coupons should be
204 disregarded.

205 ## 5. Imperfection Measurements

206 Global buckling is known to be sensitive to initial geometric imperfections and this sensitivity is typically
207 further amplified when the column fails by interaction of global and cross-sectional buckling (Van der Neut,
208 1969; Becque, 2014). For this reason, the geometric imperfections of all test specimens were recorded using a
209 specially designed imperfection measuring rig. The rig is depicted in Figure 5 and consisted of a traverse
210 system with two electric motors, which were used to move a laser sensor mounted on a trolley along high
211 precision bars in two orthogonal directions. The imperfections were measured along several longitudinal lines,
212 as shown in Figure 6. Wherever possible (and as indicated by the red arrows) measurements were taken in the
213 final assembled configuration. The black arrows indicate where measurements were taken of the individual
214 components before assembly, as access to them was restricted after the components were assembled. The
215 accuracy of the frame was assessed by verifying the repeatability of the measurements with the test specimen
216 placed in various positions within the frame and was found to be of the order of ±0.06 mm (Meza, 2018). A
217 typical measured profile is shown in Figure 7.

218 The imperfection data was further used to determine representative magnitudes of the cross-sectional out-of-
219 plane imperfections and the global imperfections of the built-up specimens. The cross-sectional imperfections

of interest included the out-of-plane imperfections along the centre line of the web measured relative to the corners (δ_{web}) and the out-of-plane imperfections along the flange edge measured relative to the corner (δ_{flange}). The 'flange edge' thereby either indicates the free edge in the case of a plain channel, or the flange-lip junction in the case of a lipped channel. When quantifying the imperfections of the flange edge, it was deemed most representative to report δ_{flange} relative to the average value along the flange of the channel. Additionally, for the lipped channels the relevant cross-sectional imperfections also included the out-of-plane imperfections along the centre line of the flanges measured relative to the corners ($\delta_{flange,L}$). Since imperfection measurements were not directly taken along the centre lines of the webs and flanges of the channels (Figure 7), these imperfections were determined using third-order polynomial interpolation based on the four imperfection readings taken on the element. Table 7 lists the maximum and the average out-of-plane imperfections recorded in each built-up geometry.

The global flexural imperfection of the built-up specimens about the major axis $\delta_{global,M}$ was computed as the average of the imperfection readings $\delta_{global,M-i}$ (i = 1 … 4), as indicated in Figure 6, evaluated at mid-height of the column. For columns LC1 $\delta_{global,M}$ was not computed, since the imperfections recorded in the plate components were not considered to be representative of the flexural imperfection of the column. Table 8 lists the global imperfections $\delta_{global,M}$ calculated for columns LC2, LC3 and LC4, with positive values indicating imperfections in the direction opposite to the applied load eccentricity.

6. Connector behaviour

The behaviour of built-up sections is generally different from the behaviour of the corresponding 'solid' section because of the finite shear stiffness of the connectors. This is particularly relevant for global instabilities which can introduce significant shear forces in the connectors. A series of single lap shear tests was therefore carried out in order to determine the actual behaviour of the connectors used to assemble the built-up columns.

The test specimens were assembled with two fasteners in the line of stress and were fabricated from steel strips taken from spare components of the built-up columns. The test set-up is illustrated in Figure 8. Three types of specimens were fabricated to cover all combinations of ply thicknesses and fastener types encountered in the built-up columns, as summarized in Table 9. The table also lists the origin of the strips.

Two identical specimens were fabricated for each configuration to countervail the natural statistical variability in the results. The steel sheets had a nominal width of 70 mm, which was reduced to 50 mm at one end in order to accommodate the specimen into the grips of the testing machine. The edge distance of the fasteners in the direction of the force and the distance between fasteners were 30 mm and 60 mm, respectively, as indicated in Figure 8. They were chosen following the recommendations given by ECCS TC7 (2009), which ensured that the behaviour of the connector was not affected by its proximity to the edge. The connector specimens were assembled, as much as possible, in the same way as the built-up specimens (for instance, applying the same torque on the bolts).

All specimens were tested in a 300 kN Shimadzu universal testing machine. Each steel sheet was packed at the end with a steel plate which had the same thickness as the adjacent steel sheet to ensure the load was applied along the shear plane. The specimens were loaded until failure at a constant displacement rate of 0.5 mm/min. The specimen deformations were recorded using two LVDTs, which were glued to the steel sheets and spring-loaded against target plates, glued to the adjacent sheet at a distance of 150 mm, as illustrated in Figure 8. One LVDT was attached to each side of the specimen in order to mitigate any error in the elongation measurements resulting from a possible initial curvature of the specimen.

Figure 9 shows the load-elongation behaviour recorded in the bolted specimens CB20-14 and CB14-14 (corresponding to the configuration in columns LC1 and LC2, respectively), and the screwed specimens CS12-12 (corresponding to columns LC3 and LC4). The curves were obtained by averaging the deformations recorded by both LVDTs.

7. Test Set-up

The columns were tested in a 2000 kN AMSLER universal testing machine. The test set-up is illustrated in Figure 10. The columns were subjected to compression between pin-ended boundary conditions, while applying the load with a nominal eccentricity of $L/1000$ or $L/1500$. A 300 kN load cell was mounted between the hydraulic actuator, located at the bottom of the set-up, and the bottom support.

The supports were designed to allow rotations about the major axis, while restraining twisting and rotations about the minor axis. They consisted of hinge assemblies of which one side was fixed to the cross-head or the actuator of the testing machine, while the other side was welded to steel bearing plates containing slotted bolt

holes. Two lines were scribed onto the sides of these steel plates. One of them lined up vertically with the axis of the hinge, while the other one was offset by the eccentricity to be applied. The bearing plates were bolted to the endplates of the column after aligning the centroid of the built-up specimen with the scribed line on the bearing plates which indicated the desired eccentricity. Fine adjustment of the position of the specimens relative to the supports was achieved by means of four adjustable screws located on the bearing plates. The accuracy of the load eccentricity was assessed by instrumenting all columns tested with a nominal eccentricity of $L/1000$ with four strain gauges at mid-height (in the locations indicated by Figure 11), and comparing the initial eccentricity at mid-height obtained from the strain gauge readings ($e_{0,SG}$) with the eccentricity ($e_{0,mid}$) obtained by adding the applied end eccentricity and the global imperfection $\delta_{\text{global,M}}$. The average difference between $e_{0,\text{SG}}$ and $e_{0,\text{mid}}$ was 0.27 mm, which proves the accuracy of the followed procedure.

The effective length of each specimen was determined as the distance between the axes of the top and bottom hinges, which amounted to $L_e = L + 147$ mm, where L is the nominal length of the column.

The columns were instrumented with six LVDTs and six potentiometers, as shown in Figure 10. The LVDTs were clamped to the pillars of the testing machine. LVDTs $T1$, $T2$, $B1$ and $B2$ were used to record the axial shortening of the columns, as well as their end rotations, while the global flexural buckling displacements at mid-height were recorded by LVDTs $G1$ and $G2$. The local buckling deformations of the component sections were recorded using potentiometers $L1$, $L2$, $L3$ and $L4$, which were mounted on individual stands attached to the bottom endplate of the specimen with magnetic bases. The potentiometers were placed at the centre of the channel webs or, in the case of geometry LC1, at the centre of the flat plate sections near the bottom of the column. In addition, in the specimens with geometries LC1, LC2 and LC3, potentiometers $W1$ and $W2$ were used to check for potential twisting of the specimen at the bottom end. The top end was not checked, as twisting of the top support was completely restrained by the cross-head of the testing machine. Readings from the potentiometers showed that no twisting occurred during the tests. In geometry LC4, potentiometers $D1$ and $D2$ were mounted on an aluminium frame, which made contact with the four corners of the cross-section and rested on three supports which were glued to three corners of the cross-section, as illustrated in Figure 12. The frame was fixed to one of the supports by hand-tightening a screw. Therefore, the frame was able to remain in place when the specimens experienced cross-sectional deformations, while moving with the cross-section as a whole when global buckling occurred. The frame was installed with the potentiometers at mid-height of the column.

All specimens were tested with a target displacement rate of 0.08 mm/min., resulting in approximate strain rates of 4.4×10^{-7} /s, 5.3×10^{-7} /s and 7.4×10^{-7} /s for the specimens with lengths of 3000 mm, 2500 mm and 1800 mm, respectively. Each test was halted for 4 minutes slightly before the peak load was reached in order to eliminate strain rate dependent effects. The displacement rate was increased past the peak load. All data was collected in a Cubus data acquisition system, using a sampling rate of 1 Hz.

8. Test results

8.1. Deformed shape

Local buckling of individual components was observed in all columns before global flexural buckling of the whole column occurred. In columns LC1 a global-type buckling of the flat plates in between connector points was also observed. As a result of the combined effects of the applied eccentricity and the initial imperfections lateral displacements of the column were seen to occur from the onset of loading. This introduced additional second order compressive stresses on one side of the column and superimposed tensile stresses on the opposite side (further referred to as the '*compression*' and '*tension*' side of the built-up specimen, respectively). Consequently, the amplitude of the local buckles in the component located on the compression side of the built-up specimen was always observed to be larger than the amplitude of the buckles in the corresponding component located on the tension side.

8.1.1 Built-up geometry 1

The columns with geometry 1 failed by global flexural buckling about the major axis of the built-up specimen, which interacted with local buckling of the channels and a global-type buckling of the flat plate components between connector points, while global flexural-torsional buckling of the channels between connectors was also observed in some columns. Columns with the same number of connectors exhibited the same initial buckled shape. However, the eventual development of a plastic yield line mechanism often occurred in different locations along the specimen height. The yield lines formed in the web and the flange of the channels located on the compression side of the built-up specimen. The deformed shapes of all the columns with geometry 1 at a load near the peak load are illustrated in Figure 13.

In columns LC1-2 and LC1-3, the relatively large connector spacing caused the flat plate components to buckle outward in each field between connectors in a global flexural mode with a half-wave length equal to

half the distance between connectors. The channels, on the other hand, buckled in a local mode, generating 22 half-waves along the column, irrespective of the number of connectors.

In columns LC1-2, the distance between connectors was large enough (960 mm) to cause failure of the channels due to flexural-torsional buckling between connectors. In the lower field of the columns both channels thereby rotated and translated towards the interior of the built-up cross-section, as shown in Figure 14, while in the central field the channels rotated and moved outwards. Flexural-torsional buckling of the channels prompted a sudden failure of the built-up specimen due to global flexural buckling.

In column LC1-3b, which had a connector spacing of 720 mm and was tested with a load eccentricity of $L/1500$, the channels also failed by flexural-torsional buckling between connectors. However, in this case both channels rotated and moved laterally in the same direction, while this direction alternated in successive fields. The tendency of the channels to twist and move laterally introduced some twisting in the already buckled plate components in the fields located directly above and below mid-height. However, no twisting of the built-up column as whole was recorded, with the specimen instead failing by global flexural buckling about the major axis. In column LC1-3a, which was tested with a larger load eccentricity ($L/1000$) than LC1-3b, but with an identical connector spacing, the channels only experienced local buckling, without any flexural-torsional deformations, as illustrated by Figure 13c. It is worth noting the difference in the plastic yield line mechanism which formed in the channels when they failed by interaction between local buckling and flexural-torsional buckling between connector points, as opposed to the one which formed when failure occurred due to interaction between local buckling of the channels and global flexural buckling of the built-up specimen. In the former, the plastic hinge mechanism developed mainly in the compression flange of the channels, as illustrated in Figure 15b for specimen LC1-3b, while in the latter yield lines also spread across the web of the channels, as shown in Figure 15a for specimen LC1-3a.

In columns LC1-8, with a shorter connector spacing, the channels were also observed to initially buckle in a local mode with multiple regular half-wave lengths along the column. However, the plate components buckled outwards in every other field along the column and remained almost straight in the adjacent fields, as the channels web prevented them from buckling inwards (Figures 13e,f). It is clear that this discontinuous buckling pattern required some slip to occur between the plate and the channels at the connector points.

8.1.2 Built-up geometry 2

All columns with geometry 2 failed by interaction between global flexural buckling about the major axis of the built-up specimen and local buckling of the individual components. Multiple regular local buckles were observed along the columns. The deformed shapes of the columns shortly before the ultimate capacity was reached are illustrated in Figure 16. Past the peak load yield lines formed in the outer channel located on the compression side of the built-up specimen, and in the web and the most compressed flange of the inner channels. A typical example of this yield line mechanism is shown in Figure 17 for column LC2-6b.

In columns LC2-2, with two rows of intermediate connectors, the outer channels were forced to mainly buckle outwards due to the presence of the inner channels, while displaying four half-waves between the connectors in the central field. This can be explained by the fact that the natural buckle half-wave length of the outer channels (considered in isolation) was calculated to be 170 mm and this was close to the 200 mm resulting from fitting four half-waves between connector points. In the adjacent fields, on the other hand, the outer channels accommodated six half-waves, with the buckle closest to the end of the column being noticeably shorter than the others. This can be attributed to the initial imperfection in the outer channel flanges resulting from welding on the endplates, as previously discussed in Section 2. The inner channels in these columns did not buckle locally before the peak load. After the ultimate capacity was reached, columns LC2-2 formed a yield line mechanism in the central connector field. At no point did the failure mechanism appear to be affected by the localized imperfections at the column ends.

Columns LC2-6 and LC2-4 had different column lengths, but similar connector spacings of 340 mm and 336 mm, respectively. Similarly to columns LC2-2, the inner channels forced the outer channels to buckle outwards and the outer channels buckled with a half-wave length equal to half the distance between connectors, as shown in Figures 16c-f. This half-wave length virtually coincided with their natural local buckle half-wave length.

As a result of the reduced connector spacing in the LC2-6 columns, the interaction between the different components was more pronounced and triggered the participation of the most compressed flange of the inner channels in the local buckling pattern near the ultimate load. The most compressed flange of the inner channels was forced to buckle towards the inside of the channel due to the presence of the outer channel webs and displayed four half-waves between connectors, as illustrated in Figures 16c-d.

In columns LC2-4 the initial distortions of the outer channel flanges at the column ends were more pronounced than in columns LC2-6. This caused the flanges of the outer channels to buckle with four half-waves between connectors in one of the fields adjacent to a column end, while in all other fields only two half-waves were observed. In both LC2-4 columns the deformations in the post-peak range localized in the end field located on the compression side of the built-up specimen where the four half-waves had previously formed, as shown in Figure 18 for column LC2-4b. It was thus clear that the presence of the welding distortions promoted the localization of the yield line mechanism, which otherwise might have formed elsewhere along the column at a slightly higher load.

8.1.3 Built-up geometry 3

All columns with geometry 3 failed by interaction between local buckling of the individual components and global flexural buckling of the built-up specimen about the major axis. A similar initial local buckling pattern was observed in each pair of columns with the same number of intermediate connectors, as illustrated in Figure 19. After reaching the ultimate capacity a plastic yield line mechanism formed with yield lines appearing in the lipped channels, the plain channel located on the compression side of the built-up specimen and the flanges of the plain channel located on the tension side, as illustrated in Figure 20 for columns LC3-2b and LC3-8b. In most columns, the yield line mechanism formed around mid-height. The only exception to this occurred in column LC3-3b, where the yield line mechanism formed near the top end of the column.

In columns LC3-2, with two intermediate sets of connectors, the lipped channels buckled locally with either ten or twelve half-waves between connectors, with the corresponding half-wave lengths ranging from 80 mm to 96 mm. The presence of the lipped channels forced the plain channels to mainly buckle outwards between connectors, with the cross-sections containing connectors always falling inside a concave buckle. Eight local half-waves were formed between connectors in the plain channels, with a half-wave length of approximately 120 mm. This buckling pattern can be explained by the fact that the natural local buckle half-wave lengths of the lipped and the plain channels (considered in isolation) were 90 mm and 130 mm, respectively.

In columns LC3-3 the connector spacing was reduced to 720 mm. In this case, the plain channels displayed six half-waves between connectors with a length of around 120 mm. The lipped channels typically buckled with eight half-waves between connectors, with a half-wave length equal to the natural local buckle half-wave

length. However, in some regions of column LC3-3a, the lipped channels were seen to buckle sympathetically with the plain channels, displaying only six half-waves between connectors.

In columns LC3-8, with a connector spacing of 320 mm, the plain and the lipped channels both buckled with either two or four half-waves between connectors and corresponding half-wave lengths of about 160 mm or about 80 mm. A half-wave length of 160 mm was preferable for the plain channels, since the signature curve of the isolated channel indicated that this corresponded to a critical stress of 81 MPa, while buckles with a half-wave length of 80 mm were associated with a critical stress of 93 MPa. For the lipped channels on the other hand, buckles with a half-wave length of 80 mm were closer to their natural local buckle half-wave length of 90 mm. Although in some fields of column LC3-8a the lipped channels and the plain channels buckled in sympathy with identical half-wave lengths, in other parts of the column this synchronisation was lost, as shown in Figure 21a. A more synchronous buckling pattern was observed in column LC3-8b, as illustrated in Figure 21b, where only a very small gap formed between the flanges of the plain channels and the web of the lipped channels as a result of local buckling.

8.1.4 Built-up geometry 4

In all columns with geometry 4 the component sections first buckled in a local mode before the column eventually failed by interaction of cross-sectional instability and global flexural buckling about the major axis. The amplitude of the local buckling pattern was always more pronounced in the lipped channel located on the compression side of the built-up specimen and also increased towards mid-height. The lipped channels were forced to mainly buckle outwards between connectors due to the presence of the plain channel webs. As a result, the cross-sections containing connectors always fell inside a concave buckle. The local buckle half-wave length in the lipped channels ranged from 80 mm to 90 mm in all columns. In columns LC4-2 this resulted in twelve half-waves between connectors in the central field and between ten and twelve in the adjacent fields, while in columns LC4-3 and LC4-8 the lipped channels displayed eight and four half-waves between connectors, respectively.

Some minor interaction with the distortional mode could also be observed in the lipped channels of columns LC4-2 and LC4-3 before the peak load was reached. This distortional buckling pattern was again more visible in the lipped channel located on the compression side of the built-up specimen. Figure 22 shows the deformed shape of all columns with geometry 4 just before the peak load was reached. Because the plain channels

prevented the web of the lipped channels from buckling towards the inside of the column, the flanges of the lipped channels were forced to deflect inwards when buckling distortionally. As the deformations localized and a yield line mechanism formed, the distortional buckling pattern became more evident. This was particularly the case in columns LC4-2b and LC4-3b, which were tested with a load eccentricity of *L*/1500, as illustrated in Figure 23a and Figure 23b, respectively.

Two distinct types of yield line mechanisms were observed in the lipped channels located on the compression side of the columns. The first yield line mechanism was dominated by the distortional mode and was spread out over a much longer region along the channel, as illustrated in Figure 24a for column LC4-2b. The second mechanism was dominated by local buckling and resulted in a much more localized pattern, as shown in Figure 24b for columns LC4-8b. In both cases, due to the influence of global flexural buckling the lipped channel located on the tension side of the built-up specimen did not form yield lines, while the plain channels only formed yield lines in the web and their most compressed flange.

8.2. Critical buckling stresses

Wherever possible, the critical buckling stresses of the various components of the built-up specimen were determined from the test results and compared to theoretical predictions. The out-of-plane deformations of the column components recorded by the potentiometers were used for this purpose and in this regard the complete data set for all columns can be found in (Meza, 2018).

The theoretical (elastic) buckling stresses of the constituent channels were calculated while considering them in isolation, using the CUFSM 4.05 software (Schafer, 2006). The measured cross-sectional dimensions (averaged over the two nominally identical components in the cross-section) and the Young's modulus obtained from the flat tensile coupons were used. The buckling pattern in the built-up sections was typically subject to the constraint that an integer number of half-waves had to fit in between the connectors. In order to take this into account in the determination of the critical buckling stress, the buckle half-wave length observed during the test was adopted in the calculations. This was achieved by reading the critical local buckling stress off the signature curve at this particular half-wave length. While this method accounted for the presence of the connectors, consideration of the channel in isolation made no allowance for the effect of contact between the

various components. Rather, a comparison between the calculated and the experimental buckling stresses provided valuable information on the extent of the restraint resulting from contact.

For the flat plate components in columns LC1, which buckled in a flexural mode in between connectors, the critical stress was determined using Euler's equation:

$$\sigma_{cr} = \frac{\pi^2 E t^2}{12 L_p^2} \tag{1}$$

where E is the Young's modulus, t is the average measured thickness of the two plate components in the column and L_p is the buckle half-wave length.

The theoretical buckling stresses of the component sections are listed in Tables 10-13 for built-up geometries 1-4, respectively. For the sake of comparison, the tables also include the natural local buckling stress of the isolated channels, determined as the first minimum in the signature curve and corresponding to a half-wave length which is not necessarily equal to the one observed in the experiment.

8.2.1 Built-up geometry 1

In the columns with geometry 1 the flat plate components buckled in a flexural mode between connectors before local buckling of the channels occurred. Assuming that the load was initially uniformly distributed over all components of the built-up cross-section, the experimental buckling stress of the plates could be obtained by dividing the load at which buckling of the plates was observed over the total area of the built-up section. The buckling stress of the channels, on the other hand, was determined from their observed buckling load by taking into account that the global flexural buckling mode has negligible post-buckling capacity and that the plate components were therefore unable to carry any further load increment after they buckled.

The potentiometers consistently recorded that the plate component located on the compression side of the built-up specimen buckled slightly before the one on the tension side, as illustrated in Figure 25 for column LC1-2b, and the critical buckling stress was taken as the average value.

The experimental buckling stresses of the components are compared to the theoretical ones in Table 10, which also lists the buckle half-wave lengths observed during the tests. The buckle half-wave length of the plate components was assumed to be equal to half the distance between the connectors for the purpose of applying Eq. (1), since this most closely resembled the experimental observations. In columns LC1-2 and LC1-3 the

experimental buckling stress of the plates exceeded the theoretically predicted stress by 2-3 MPa. This can be explained by the fact that the plates were observed to buckle first in the top field, where no potentiometers were present to record the out-of-plane deformations. Consequently, buckling was only recorded at a subsequently increased load. In columns LC1-8 the experimentally determined buckling stresses of the plates were slightly below the theoretically calculated ones. The experimentally derived buckling stresses of the channels, on the other hand, were around 8 % larger than the theoretically predicted values in columns LC1-2 and LC1-3 (which virtually coincided with the natural local buckling stress of the channel), while for columns LC1-8 they were 11 % larger than the natural local buckling stress. This indicated a minor amount of local buckling restraint on the channels as a result of these being part of the built-up cross-section.

8.2.2 Built-up geometry 2

In the columns with geometry 2 the outer channels buckled first in a local mode, before buckling of the inner channels occurred. Since local buckling has a significant, yet not easily quantifiable post-bucking load-bearing capacity, only the critical buckling stress of the outer channels could be determined from the experiments. This critical stress was obtained assuming that, prior to buckling, the load was uniformly distributed over the built-up cross-section.

Table 11 shows the theoretical critical buckling stresses of the inner and outer channels, their experimentally observed half-wave lengths and the experimentally determined buckling stresses of the outer channels. Despite the fact that the outer channels typically buckled with a half-wave length nearly equal to the natural local buckle half-wave length, their experimentally observed buckling stresses were on average 26 % larger than the natural local buckling stress of the isolated unrestrained channel. This demonstrates that the outer channels received a substantial amount of restraint from the inner channels against local buckling.

8.2.3 Built-up geometry 3

In columns LC3-2 and LC3-3 the plain channels buckled before the lipped channels, while in columns LC3-8 all components buckled at approximately the same time. This allowed the determination of the buckling stress of the lipped channels in columns LC3-8, as well as the buckling stress of the plain channels in all columns, assuming a uniform stress distribution before buckling. Table 12 lists the theoretical and experimental critical buckling stresses of the lipped and the plain channels, as well as their buckle half-wave lengths observed during the tests. In columns LC3-8 the components were seen to buckle with two different half-wave lengths,

519 as previously explained in Section 8.1.3, and the stress associated with each half-wave length is included in
520 the table.

521 In columns LC3-2 and LC3-3 the plain channels were observed to buckle at stress levels which were 31 % and
522 22% higher than the theoretical predictions, respectively. This is indicative of the high level of restraint which
523 the plain channels received from the lipped channels in these columns. The same conclusion can be drawn for
524 the plain channels in the LC3-8 columns, while the lipped channels in the LC3-8 columns were observed to
525 buckle near the low end of the theoretically predicted range.

526 **8.2.4 Built-up geometry 4**

527 The plain channels buckled before the lipped channels in all columns with geometry 4, which allowed the
528 determination of their buckling stress from the potentiometer readings. The results are listed in Table 13,
529 which also includes the buckle half-wave length observed in the lipped channels during the tests. Since the
530 geometric arrangement of the components in the columns with geometry 4 prevented direct observation of the
531 buckle half-wave length of the plain channels during the tests, for the purpose of determining the theoretical
532 buckling stress the half-wave length was assumed to be identical to the one observed in the plain channels of
533 columns LC3 (which had identical nominal dimensions and connector spacings).

534 Table 13 shows that the critical buckling stresses of the plain channels derived from the experiment were on
535 average 7 % larger than the theoretical predictions and 11 % larger than the natural local buckling stress of the
536 unrestrained channel. However, the connector spacing did not seem to significantly affect the buckling stress.

537 It is worth noting that in columns LC4-2b and LC4-3b the critical buckling stresses of the plain channels were
538 slightly lower than those measured in the corresponding columns LC4-2a and LC4-3a. This is thought to be
539 related to the fact that in columns LC4-2b and LC4-3b, unlike in the other LC4 columns, distortional bucking
540 of the lipped channels occurred at approximately the same load as local buckling of the plain channels.

541 **8.3. Ultimate loads**

542 The load vs. axial displacement curves of all columns are plotted in Figures 26-29 and the corresponding
543 ultimate loads are listed in Table 14. ‘Static’ values are reported, obtained by allowing the load to settle near
544 the peak of the curve.

8.3.1 Built-up geometry 1

Table 14 shows that the ultimate capacity of the columns tested with a load eccentricity of *L*/1500 was on average marginally larger (by 1.8 %) than the ultimate capacity of the corresponding columns tested with a load eccentricity of *L*/1000. Regarding the effect of the connector spacing, only columns LC1-8, with a connector spacing of 320 mm, showed a noticeable increase in the ultimate capacity (of 15.1 %) with respect to columns LC1-2, which had a connector spacing of 960 mm. The ultimate capacity of columns LC1-3, with a connector spacing of 720 mm, was only 2.7 % larger than that of columns LC1-2.

8.3.2 Built-up geometry 2

As previously discussed in Section 7.1.2, failure of the shortest columns with geometry 2 (LC2-4) was promoted by larger than typical imperfections near the column ends resulting from welding distortions and this should be taken into account when interpreting the results. For the rest of columns, however, Table 14 shows that reducing the connector spacing from 793 mm (LC2-2) to 340 mm (LC2-6) did not result in a noticeable increase in the ultimate capacity. Regarding the effect of the load eccentricity, columns LC2-2b and LC2-6b, which were tested with a load eccentricity of *L*/1500, showed increases in their ultimate capacity of 6.6 % and 1.0 % with respect to their counterparts LC2-2a and LC2-6a, respectively.

8.3.3 Built-up geometry 3

Table 14 shows that a smaller load eccentricity generally resulted in a slightly higher capacity, as expected. For example, the ultimate capacities of columns LC3-2b and LC3-3b were on average 3.6 % larger than the ultimate capacities of columns LC3-2a and LC3-3a. The only exception occurred in columns LC3-8, where the ultimate capacity of column LC3-8b was 0.6 % lower than that of column LC3-8a. This can likely be attributed to a cable acquiring the load cell data becoming faulty while testing column LC3-8b, and therefore it is cautiously advised that the peak load value of this column be disregarded. The tests generally showed that reducing the connector spacing resulted in a negligible increment in the ultimate capacity. For example, the gain in ultimate capacity when reducing the connector spacing from 960 mm in column LC3-2a to 320 mm in column LC3-8a was only 0.5 %, while the ultimate capacity of columns LC3-3, with a connector spacing of 720 mm, was on average 0.1 % lower than that of columns LC3-2.

571 **8.3.4 Built-up geometry 4**

572 Regarding the columns with geometry 4, Table 14 shows that columns LC4-2b, LC4-3b and LC4-8b, with
573 eccentricities of *L*/1500, achieved peak loads which were 1.2 %, 2.1 % and 9.7 % higher than those of
574 columns LC4-2a, LC4-3a and LC4-8a, respectively, with eccentricities of *L*/1000. The effect of the connector
575 spacing on the ultimate capacity was negligible, with a mere 0.7 % increase when reducing the connector
576 spacing from 960 mm to 320 mm, and a 0.3 % increase when reducing the connector spacing from 960 mm to
577 720 mm.

578 ## 9. Conclusions

579 A comprehensive experimental programme consisting of 24 built-up columns with four different cross-
580 sectional geometries was carried out. The overall aim of the programme was to investigate the behaviour,
581 stability and ultimate capacity of built-up CFS columns and quantify the effects of connector spacing and
582 contact between the individual components.

583 The built-up sections were fabricated from flat plates, plain channels and lipped channels and were assembled
584 with either bolts or self-drilling screws. The connector spacing was varied between specimens of the same
585 cross-sectional geometry. All columns were tested between pin-ended boundary conditions about the major
586 axis with load eccentricities of *L*/1000 or *L*/1500. Coupon tests were carried out to determine the material
587 properties of the flat portions and corner regions of the components and detailed measurements of the
588 geometric imperfections of the test specimens were also taken. In addition, the isolated behaviour of both the
589 bolts and the screws used in the specimens was investigated through single lap shear tests.

590 All columns were observed to fail by interaction between cross-sectional instability of the components and
591 global flexural buckling about the major axis of the built-up column, while a global-type buckling of the
592 components in between connector points also occurred in some columns.

593 The observed cross-sectional buckling patterns in the components of the columns were significantly different
594 from those expected in the isolated components as a result of contact between the components (which often
595 forced the out-of-plane displacements to exclusively occur in one direction) and the need to synchronize the
596 buckle half-wave length with the connector spacing. The corresponding increases in the buckling stress were
597 rather modest and ranged between 11 % and 34%.

598 Provided that buckling of the components in between connector points is not critical, the test indicated that the
599 connector spacing has an almost negligible effect on the ultimate strength of the column. It should be noted
600 that connector spacings shorter than the local buckle half-wave length were excluded for practical reasons.

601 ## Acknowledgement

602 The authors are grateful for the financial support provided by the EPSRC through grant EP/M011976/1.

603 ## References

604 AISI (2016), *North American Specification for the Design of Cold-Formed Steel Structural Members*.

605 Becque, J. (2014), "Local-overall interaction buckling of inelastic columns: A numerical study of the inelastic
606 Van der Neut column", *Thin-Walled Structures*. 81, 101–107.

607 CEN (2006), Eurocode 3 — Design of steel structures — Part 1-3: General rules — Supplementary rules for
608 cold-formed members and sheeting, British Standard Institution.

609 CEN (2009), BS EN ISO 6892-1:2009 - Metallic materials — Tensile testing — Part 1 : Method of test at
610 ambient temperature, British Standard Institution.

611 ECCS TC7 (2009), The Testing of Connections with Mechanical Fasteners in Steel Sheeting and Sections.

612 Fratamico, D.C., Torabian, S., Zhao, X., Rasmussen, K.J.R. and Schafer, B.W. (2018), "Experiments on the
613 global buckling and collapse of built-up cold-formed steel columns", *Journal of Constructional Steel*
614 *Research*, 144, 65–80.

615 Georgieva, I., Schuerermans, L., Roeck, G. De and Pyl, L. (2011), "Experimental Investigation of the
616 Deformation of Built-up Members of Cold-formed Steel Profiles", *Applied Mechanics and Materials*,
617 70, 416–421.

618 Georgieva, I., Schueremans, L. and Pyl, L. (2012a), "Composed columns from cold-formed steel Z-profiles:
619 Experiments and code-based predictions of the overall compression capacity", *Engineering Structures*,
620 37, 125–134.

621 Georgieva, I., Schueremans, L., Pyl, L. and Vandewalle, L. (2012b), "Experimental investigation of built-up
622 double-Z members in bending and compression", *Thin-Walled Structures*, 53, 48–57.

623 Georgieva, I., Schueremans, L., Pyl, L. and Vandewalle, L. (2012c), "Numerical study of built-up double-Z
624 members in bending and compreassion", *Thin-Walled Structures*, 60, 85–97.

625 Huang, Y., and Young, B. (2014). "The art of coupon tests", *Journal of Constructional Steel Research*, 96,
626 159-175.

627 Lu, Y., Zhou, T., Li, W. and Wu, H. (2017), "Experimental investigation and a novel direct strength method
628 for cold-formed built-up I-section columns", *Thin-Walled Structures*, 112, 125–139.

629 Meza, F.J. (2018), "The Behaviour of Cold-Formed Steel Built-up Structural Members", PhD thesis, The
630 University of Sheffield, UK.

631 Meza, F., Becque, J., Hajirasouliha, I. (2015), "Experimental Investigation of Cold-Formed Steel Built-up
632 Stub Columns", *Eighth International Conference on Advances in Steel Structures*, Lisbon, Portugal.

633 Meza, F.J., Becque, J. and Hajirasouliha, I. (2019), "Experimental study of cold-formed steel built-up stub
634 columns", *Engineering Structures*, [To be submitted].

635 Reyes, W. and Guzmán, A. (2011), "Evaluation of the slenderness ratio in built-up cold-formed box sections",
636 *Journal of Constructional Steel Research*, 67, 929–935.

637 Schafer, B.W. (2006), "Buckling analysis of cold-formed steel members using CUFSM : conventional and
638 constrained finite strip methods", *18th International Specialty Conference on Cold-Formed Steel*
639 *Structures*, Orlando, Florida.

640 Stone, T.A. and LaBoube, R.A. (2005), "Behavior of cold-formed steel built-up I-sections", *Thin-Walled*
641 *Structures*, 43, 1805–1817.

642 Van der Neut, A. (1969), "The interaction of local buckling and column failure of thin-walled compression
643 members", *Proceedings 12th International Congress of Applied Mechanics*. pp. 389–399.

644 Whittle, J. and Ramseyer, C. (2009), "Buckling capacities of axially loaded, cold-formed, built-up C-
645 channels", *Thin-Walled Structures*, 47, 190–201.

646 Young, B. and Chen, J. (2008), "Design of Cold-Formed Steel Built-Up Closed Sections with Intermediate
647 Stiffeners", *Journal of Structural Engineering*, 134, 727–737.

648 Zandonini, R. (1985), "Stability of compact built-up struts: experimental investigation and numerical
649 simulation", *Construzioni Metalliche*. No. 4, 1985.

650 Zhang, J.-H. and Young, B. (2012), Compression tests of cold-formed steel I-shaped open sections with edge
651 and web stiffeners, *Thin-Walled Structures*, 52, 1–11.

652 Zhang, J. and Young, B. (2015), "Numerical investigation and design of cold-formed steel built-up open
653 section columns with longitudinal stiffeners", *Thin Walled Structures*, 89, 178–191.

654 Zhang, J.H. and Young, B. (2018), "Experimental investigation of cold-formed steel built-up closed section
655 columns with web stiffeners" *Journal of Constructional Steel Research*, 147, 380–392.

Table 1: Nominal dimensions of the component cross-sections

Column	section	h (mm)	b (mm)	l (mm)	t (mm)	r_{int} (mm)
LC1	T13014	130	35	-	1.4	2.8
	P15020	150	-	-	2.0	-
LC2	T15414	154	54	-	1.4	2.8
	T7914	79	36	-	1.4	2.8
LC3/LC4	T12012	120	40	-	1.2	2.4
	S11012	110	50	10	1.2	2.4

Table 2: Measured dimensions of built-up column 1

Column	Channels				Plates		
	component	h (mm)	b (mm)	t (mm)	component	h (mm)	t (mm)
LC1-2a	T13014-1	129.64	35.85	1.381	P15020-1	149.91	1.962
	T13014-2	129.70	35.91	1.382	P15020-2	149.87	1.929
LC1-2b	T13014-3	129.87	35.79	1.375	P15020-3	150.18	1.964
	T13014-4	130.11	35.81	1.368	P15020-4	149.86	1.959
LC1-3a	T13014-5	129.92	35.97	1.377	P15020-5	150.01	1.957
	T13014-6	129.92	35.88	1.380	P15020-6	149.82	1.962
LC1-3b	T13014-7	129.87	35.89	1.373	P15020-7	150.02	1.956
	T13014-8	129.96	35.86	1.370	P15020-8	149.75	1.928
LC1-8a	T13014-9	129.75	35.99	1.388	P15020-9	150.02	1.963
	T13014-10	129.86	35.96	1.386	P15020-10	149.85	1.955
LC1-8b	T13014-11	129.93	35.89	1.373	P15020-11	149.97	1.949
	T13014-12	129.84	35.94	1.382	P15020-12	149.94	1.948
Average	T13014	129.87	35.90	1.378	P15020	149.93	1.953
St. Dev.	T13014	0.124	0.062	0.006	P15020	0.115	0.012

Table 3: Measured dimensions of built-up column 2

Column	Outer channels				Inner channels			
	component	h (mm)	b (mm)	t (mm)	component	h (mm)	b (mm)	t (mm)
LC2-2a	T15414(l)-1	153.72	54.43	1.403	T7914-1	78.93	36.87	1.373
	T15414(l)-2	153.86	54.37	1.386	T7914-2	79.00	36.88	1.368
LC2-2b	T15414(l)-3	153.88	54.37	1.381	T7914-3	79.09	36.83	1.459
	T15414(l)-4	153.67	54.43	1.404	T7914-4	79.05	36.88	1.375
LC2-6a	T15414(l)-5	153.79	54.28	1.399	T7914-5	79.02	36.91	1.375
	T15414(l)-6	153.71	54.34	1.399	T7914-6	78.73	36.90	1.373
LC2-6b	T15414(l)-7	153.91	54.40	1.393	T7914-7	78.87	36.68	1.360
	T15414(l)-8	153.86	54.41	1.378	T7914-8	78.95	36.83	1.369
LC2-4a	T15414(s)-9	153.77	54.13	1.368	T7914-9	79.63	36.31	1.366
	T15414(s)-10	153.84	54.09	1.377	T7914-10	79.12	36.71	1.372
LC2-4b	T15414(s)-11	153.73	54.31	1.381	T7914-11	79.20	36.81	1.371
	T15414(s)-12	153.73	54.21	1.383	T7914-12	79.26	36.79	1.364
Average	T15414(l)	153.80	54.38	1.393	T7914	79.07	36.78	1.377
	T15414(s)	153.77	54.19	1.377				
St. Dev.	T15414(l)	0.090	0.051	0.010	T7914	0.227	0.165	0.026
	T15414(s)	0.052	0.097	0.007				

Table 4: Measured dimensions of built-up column 3

Column	Plain channels				Lipped channels				
	component	*h* (mm)	*b* (mm)	*t* (mm)	component	*h* (mm)	*b* (mm)	*l* (mm)	*t* (mm)
LC3-2a	T12012-1	119.67	39.92	1.101	S11012-1	108.98	49.50	9.62	1.100
	T12012-2	119.21	39.86	1.103	S11012-2	109.21	49.50	9.62	1.096
LC3-2b	T12012-3	119.39	39.91	1.107	S11012-3	109.54	49.61	9.70	1.108
	T12012-4	119.57	40.05	1.109	S11012-4	108.99	49.75	9.71	1.102
LC3-3a	T12012-5	119.61	40.03	1.104	S11012-5	110.14	49.71	9.73	1.093
	T12012-6	119.62	40.10	1.110	S11012-6	109.27	49.76	9.75	1.103
LC3-3b	T12012-7	119.65	40.06	1.107	S11012-7	109.18	49.55	9.80	1.104
	T12012-8	119.62	40.04	1.112	S11012-8	109.66	49.74	9.86	1.104
LC3-8a	T12012-9	119.60	40.00	1.104	S11012-9	109.32	50.04	9.96	1.102
	T12012-10	119.62	40.03	1.109	S11012-10	109.71	50.06	9.98	1.100
LC3-8b	T12012-11	119.23	39.83	1.112	S11012-11	109.65	49.97	10.03	1.105
	T12012-12	119.19	39.73	1.115	S11012-12	109.78	49.85	9.97	1.104
Average	T12012	119.50	39.96	1.108	S11012	109.45	49.75	9.81	1.102
St. Dev.	T12012	0.188	0.113	0.004	S11012	0.351	0.198	0.145	0.004

Table 5: Measured dimensions of built-up column 4

Column	Plain channels				Lipped channels				
	component	*h* (mm)	*b* (mm)	*t* (mm)	component	*h* (mm)	*b* (mm)	*l* (mm)	*t* (mm)
LC4-2a	T12012-13	119.15	39.72	1.113	S11012-13	109.89	49.85	9.97	1.097
	T12012-14	119.19	39.78	1.107	S11012-14	109.37	49.84	9.88	1.107
LC4-2b	T12012-15	119.29	39.73	1.102	S11012-15	109.24	49.75	9.96	1.108
	T12012-16	119.29	39.75	1.103	S11012-16	110.86	49.77	9.22	1.110
LC4-3a	T12012-17	119.12	39.69	1.100	S11012-17	109.47	49.80	9.80	1.108
	T12012-18	119.17	39.74	1.102	S11012-18	109.17	49.77	9.82	1.107
LC4-3b	T12012-19	119.17	39.80	1.110	S11012-19	109.88	49.79	9.81	1.091
	T12012-20	119.24	39.69	1.108	S11012-20	109.27	49.93	9.75	1.104
LC4-8a	T12012-21	119.18	39.67	1.108	S11012-21	109.66	49.82	9.82	1.096
	T12012-22	119.29	39.62	1.108	S11012-22	110.21	49.71	9.70	1.097
LC4-8b	T12012-23	119.29	39.60	1.102	S11012-23	109.06	49.78	9.88	1.102
	T12012-24	119.11	39.71	1.110	S11012-24	108.93	49.98	9.83	1.106
Average	T12012	119.21	39.71	1.106	S11012	109.58	49.82	9.79	1.103
St. Dev.	T12012	0.070	0.060	0.004	S11012	0.553	0.077	0.194	0.006

Table 6: Material properties of tensile coupons

coupon	Section	*E* (GPa)	$\sigma_{0.2\%}$ (MPa)	σ_u (MPa)	ε_f (%)
Flat	P15020	206	260	357	26
Flat	T13014	199	279	340	35
Flat	T15414(l)*	207	325	388	27
Flat	T15414(s)**	198	280	341	34
Flat	T7914	203	281	339	35
Flat	T12012	192	242	320	31
Flat	S11012	198	277	357	28
Corner	T13014	-	347	379	12
Corner	T15414(l)*	-	410	429	(6)
Corner	T15414(s)**	-	362	395	12
Corner	T7914	-	344	383	13
Corner	T12012	-	311	353	16
Corner	S11012	-	346	384	12

*= LC2-2 and LC2-6 columns; **= LC2-4 columns

Table 7: Maximum and average measured cross-sectional imperfections

Specimen	Section	Imperfection (mm)		
			Max.	Avg.
LC1	T15414	δ_{web}	0.48	0.14
LC2	T7912	δ_{web}	0.59	0.04
	T15414	δ_{web}	0.58	0.15
		δ_{flange}	0.96	-
LC3	T12012	δ_{web}	0.61	0.08
		δ_{flange}	0.65	-
	S11012*	δ_{web}	0.41	0.04
LC4	S11012	δ_{web}	0.41	0.07
		δ_{flange}	1.12	-
		$\delta_{flange,L}$	0.15	0.02
	T12012*	δ_{web}	0.25	0.05
*Imperfections recorded before the sections were assembled				

Table 8: Measured major axis global imperfection

Specimen	$\delta_{global,M}$	
	(mm)	(-)
LC2-2a	0.081	L/33000
LC2-2b	-0.169	-L/16000
LC2-6a	0.010	L/265000
LC2-6b	0.242	L/11000
LC2-4a	0.099	L/20000
LC2-4b	0.134	L/15000
LC3-2a	-0.258	-L/12000
LC3-2b	-0.098	-L/32000
LC3-3a	0.032	L/98000
LC3-3b	-0.323	-L/10000
LC3-8a	-0.379	-L/8000
LC3-8b	0.249	L/13000
LC4-2a	-0.068	-L/46000
LC4-2b	-0.147	-L/21000
LC4-3a	-0.017	-L/185000
LC4-3b	0.197	L/16000
LC4-8a	0.128	L/25000
LC4-8b	-0.125	-L/25000

Table 9: Connector test specimens

Specimen	Connector type	Ply 1: thickness (mm)	Ply 1: corresponding component	Ply 2: thickness (mm)	Ply 2: corresponding component
CB14-14a	8.8 M6 bolts	1.447	T15414	1.404	T7914
CB14-14b	8.8 M6 bolts	1.451	T15414	1.406	T7914
CB20-14a	8.8 M6 bolts	1.977	P15020	1.398	T13014
CB20-14b	8.8 M6 bolts	1.976	P15020	1.405	T13014
CS12-12a	M5.5 screws	1.137	T12012	1.115	S11012
CS12-12b	M5.5 screws	1.138	T12012	1.112	S11012

Table 10: Buckling stresses of the components of geometry 1

Column	Min. theoretical buckling stress (MPa)	Experimental half-wave length (mm)	Theoretical buckling stress (MPa)		Experimental buckling stress (MPa)	
	Channel	Channel	Channel	Plate	Channel	Plate
LC1-2a	93	131	93	3	99	6
LC1-2b	91	131	91	3	98	5
LC1-3a	92	131	92	5	97	8
LC1-3b	91	131	91	5	101	8
LC1-8a	93	-	-	25	100	23
LC1-8b	92	-	-	25	106	23

Table 11: Buckling stresses of the components of geometry 2

Column	Min. theoretical buckling stress (MPa)		Experimental half-wave length (mm)		Theoretical buckling stress (MPa)		Experimental buckling stress (MPa)	
	Inner Channel	Outer Channel	Inner Channel	Outer Channel	Inner Channel	Outer Channel	Inner Channel	Outer Channel
LC2-2a	182	64	-	198	-	66	-	83
LC2-2b	182	64	-	198	-	66	-	77
LC2-6a	183	64	85	170	187	64	-	74
LC2-6b	181	63	85	170	185	63	-	78
LC2-4a	183	59	-	168	-	59	-	83
LC2-4b	181	60	84	168	185	60	-	76

Table 12: Buckling stresses of the different components of geometry 3

Column	Min. theoretical buckling stress (MPa)		Experimental half-wave length (mm)		Theoretical buckling stress (MPa)		Experimental buckling stress (MPa)	
	Plain Channel	Lipped Channel	Plain Channel	Lipped Channel	Plain Channel	Lipped Channel	Plain Channel	Lipped Channel
LC3-2a	63	103	120	80-96	63	103-105	82	-
LC3-2b	64	104	120	80-96	64	104-106	84	-
LC3-3a	64	102	120	90-120	64	102-115	77	-
LC3-3b	64	104	120	90	64	104	79	-
LC3-8a	63	103	80-160	80-160	75-66	103-148	82-105	99
LC3-8b	65	103	80-160	80-160	77-67	104-148	88-109	109

Table 13: Buckling stresses of the components of geometry 4

Column	Min. theoretical buckling stress (MPa)		Experimental half-wave length (mm)		Theoretical buckling stress (MPa)		Experimental buckling stress (MPa)	
	Plain Channel	Lipped Channel	Plain Channel	Lipped Channel	Plain Channel	Lipped Channel	Plain Channel	Lipped Channel
LC4-2a	64	103	-	80-96	64	103-104	74	-
LC4-2b	64	103	-	80-96	64	104-105	63	-
LC4-3a	64	104	-	90	64	105	78	-
LC4-3b	64	102	-	90	65	102	73	-
LC4-8a	66	101	-	80	68-77	102	63-85	-
LC4-8b	64	104	-	80	66-76	105	67	-

Table 14: Ultimate loads

Geometry 1		Geometry 2		Geometry 3		Geometry 4	
Column	Ultimate load (kN)	Column	Ultimate load (kN)	Column	Ultimate load (kN)	Column	Ultimate load (kN)
LC1-2a	77.94	LC2-2a	160.90	LC3-2a	119.04	LC4-2a	116.53
LC1-2b	79.18	LC2-2b	171.82	LC3-2b	123.48	LC4-2b	117.90
LC1-3a	79.73	LC2-6a	165.15	LC3-3a	118.88	LC4-3a	116.19
LC1-3b	81.57	LC2-6b	166.88	LC3-3b	122.94	LC4-3b	118.57
LC1-8a	89.66	LC2-4a	162.31	LC3-8a	120.22	LC4-8a	109.06
LC1-8b	91.17	LC2-4b	173.37	LC3-8b	(119.54)	LC4-8b	119.65

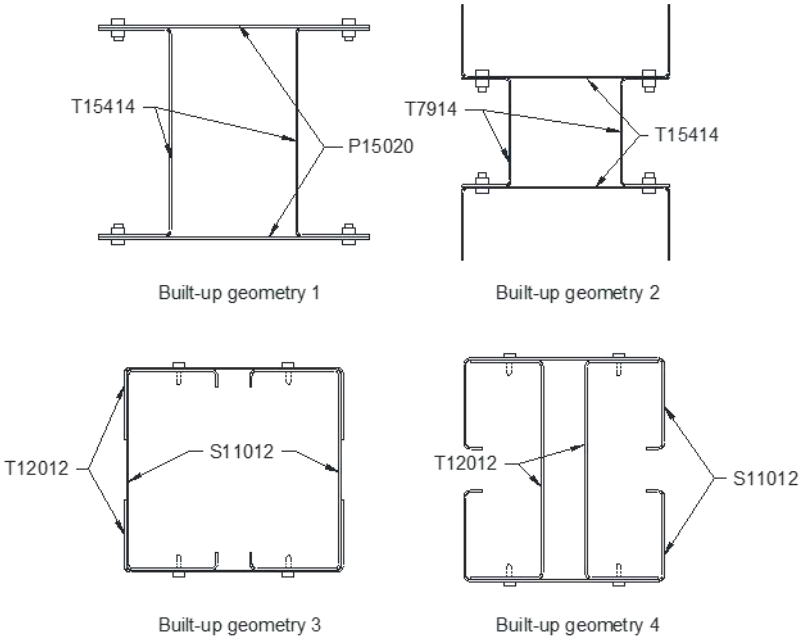

Figure 1: Built-up cross sections

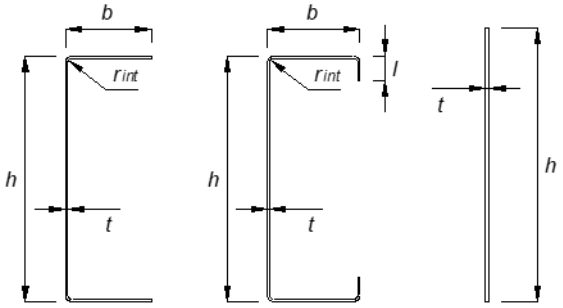

Figure 2: Nomenclature for the dimensions of the component cross-sections

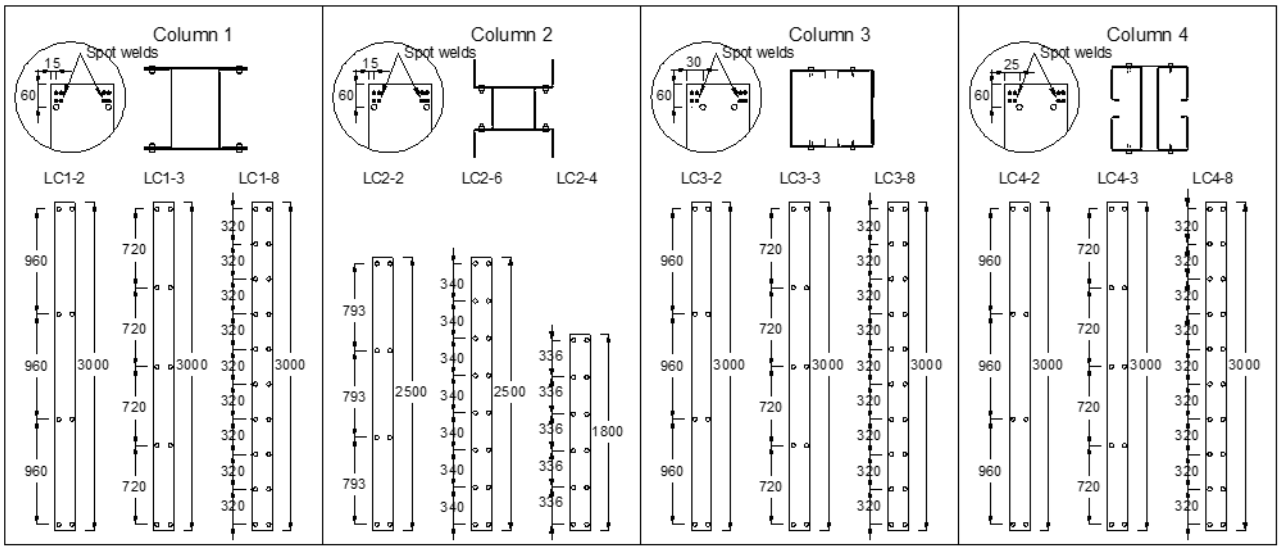

Figure 3: Location of connectors

Figure 4: End plate and typical flange distortion of channel T15414 in specimen LC2-4b

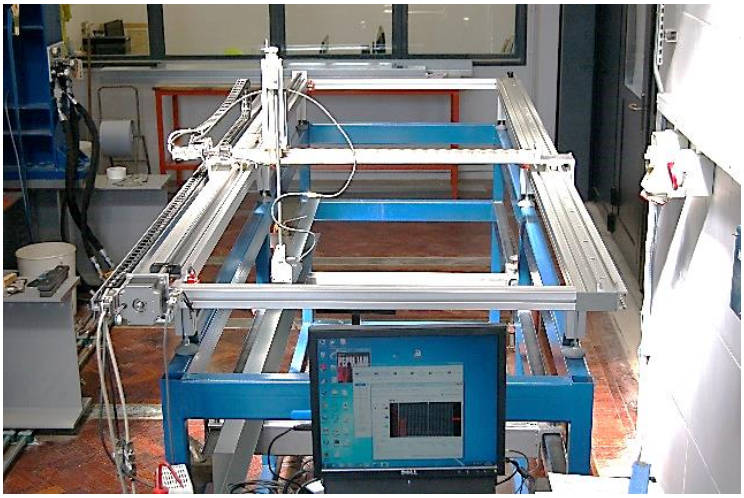

Figure 5: Imperfection measuring rig

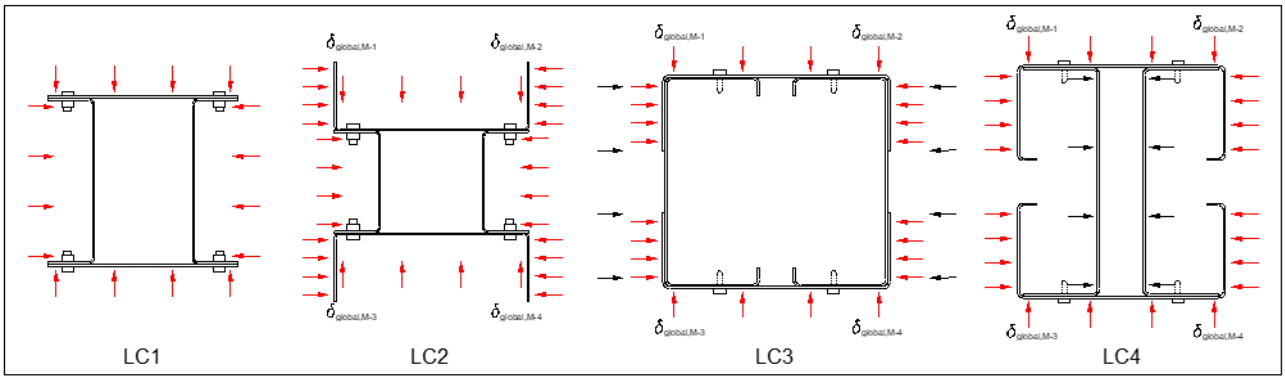

Figure 6: Location of the imperfection measurements

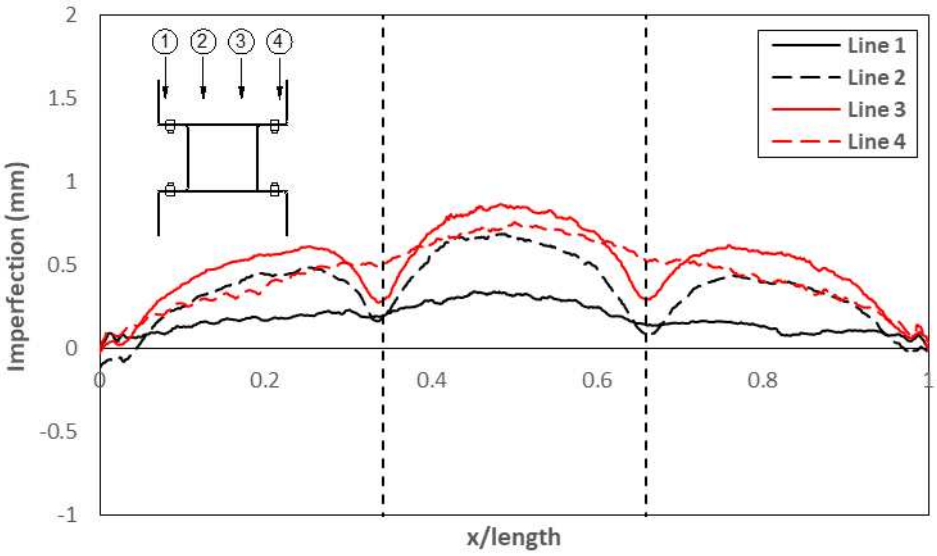

Figure 7: Imperfections recorded along the web of channel T15414-3 in column LC2-2a

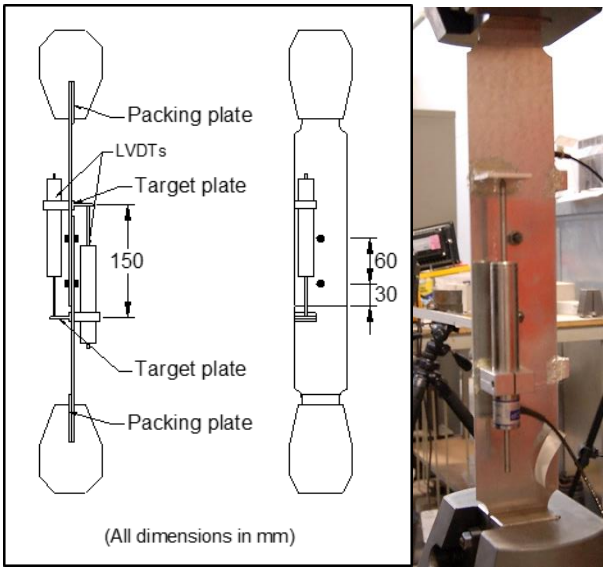

Figure 8: Single lap shear test set-up

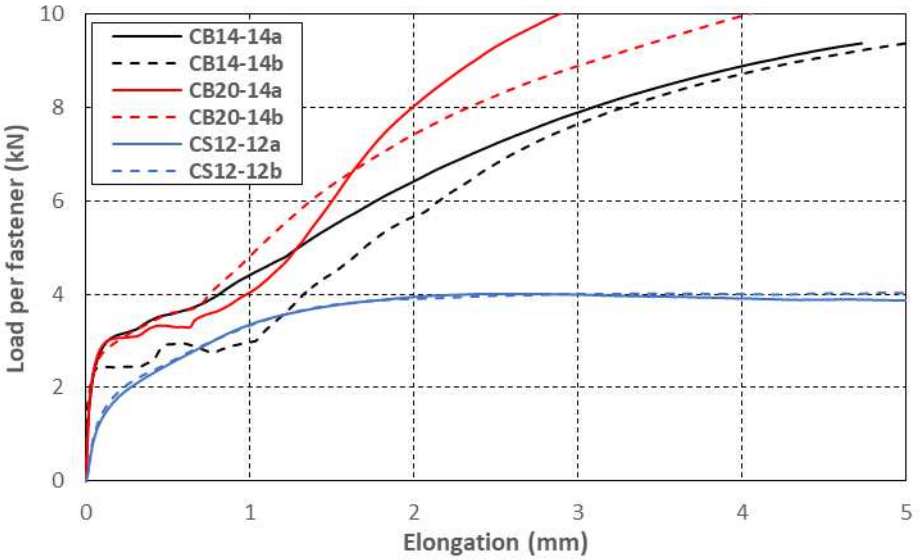

Figure 9: Load-elongation behaviour of connectors

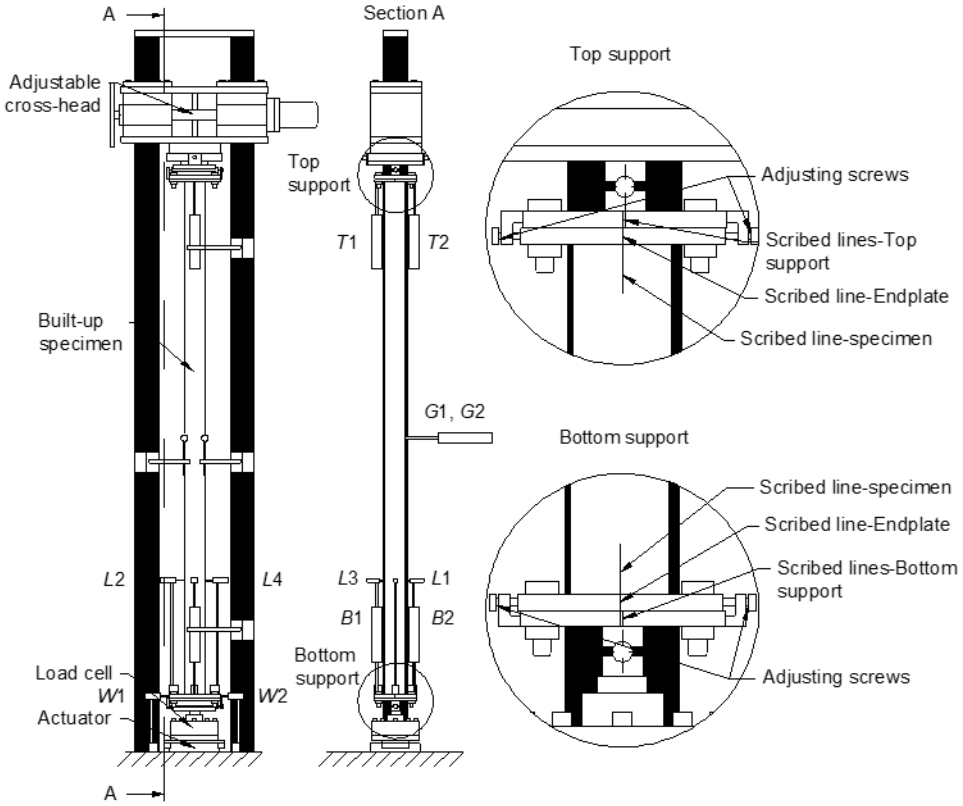

Figure 10: Test set-up

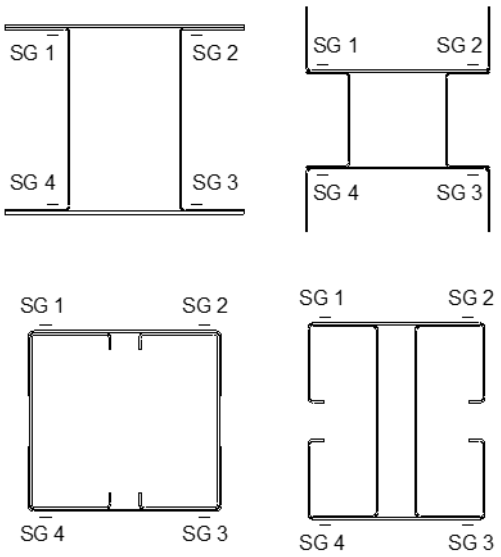

Figure 11: Strain gauge locations

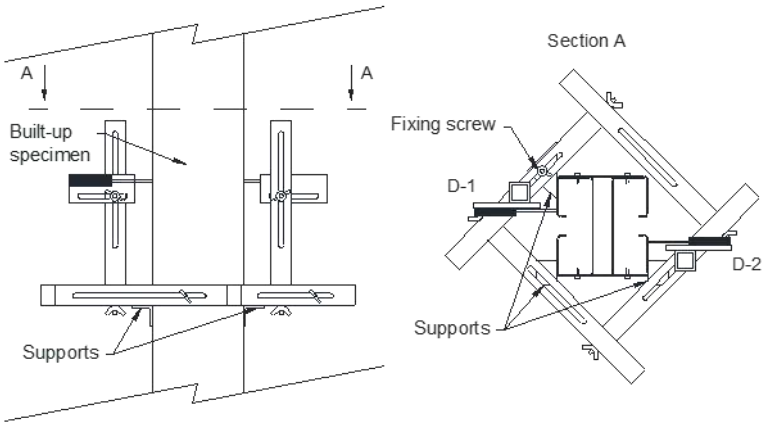

Figure 12: Schematic representation of the aluminium frame holding potentiometers *D*1 and *D*2

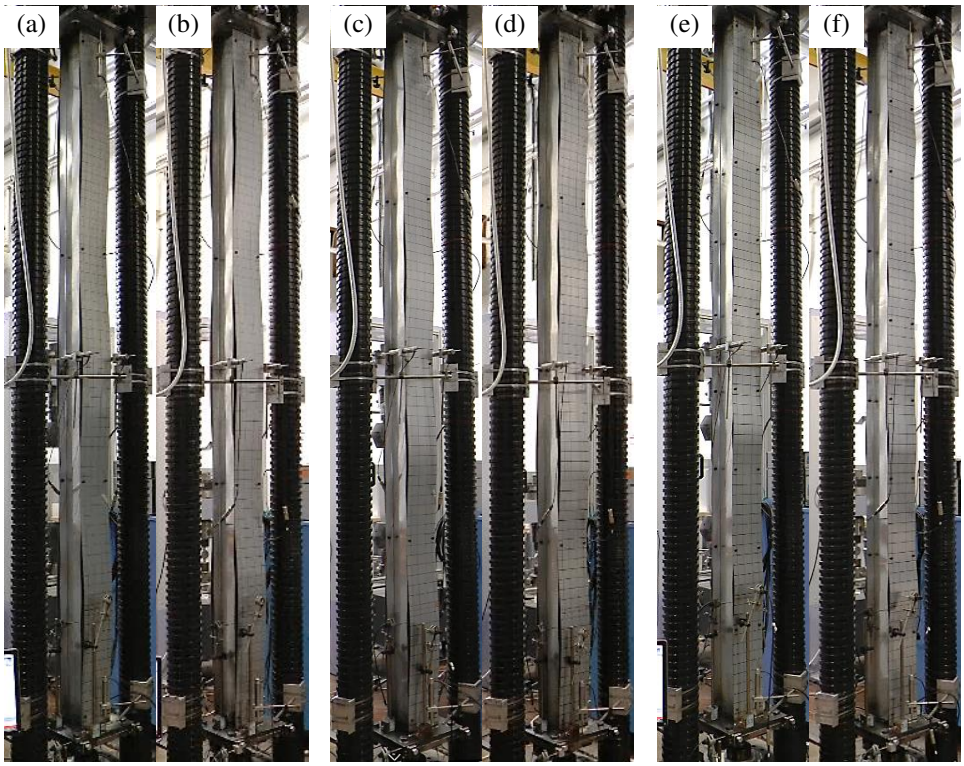

Figure 13: Deformed shape approaching ultimate load in a) LC1-2a, b) LC1-2b, c) LC1-3a, d) LC1-3b, e) LC1-8a, f) LC1-8b

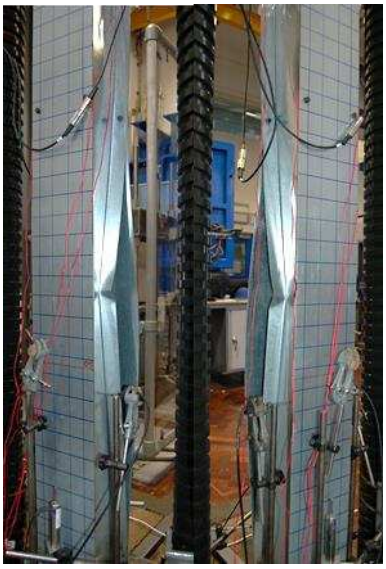

Figure 14: Failed shape of column LC1-2a, observed from both sides of the column

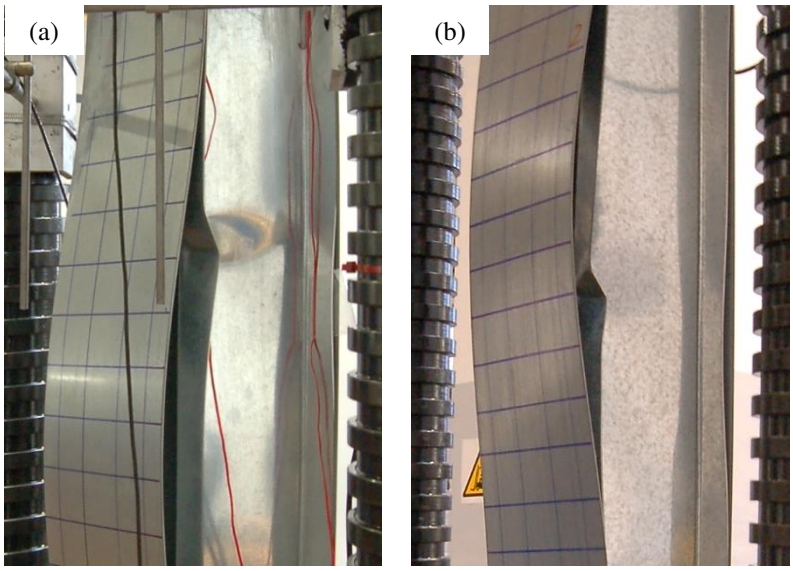

Figure 15: Plastic yield line mechanism in a) LC1-3a, b) LC1-3b

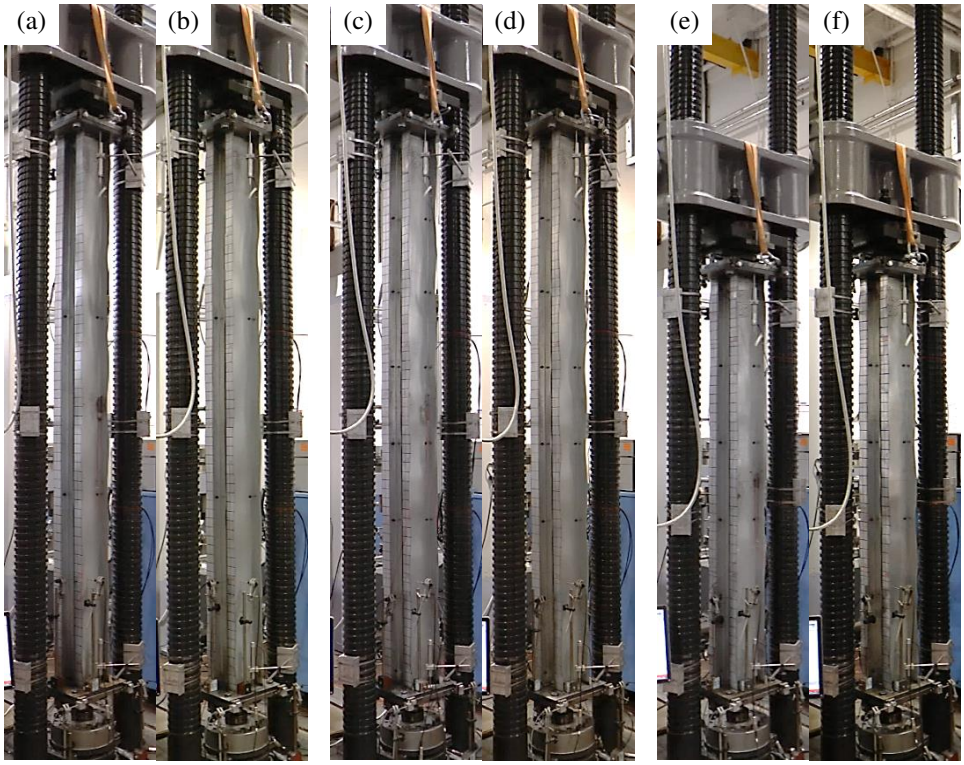

Figure 16: Deformed shape approaching ultimate load in a) LC2-2a, b) LC2-2b, c) LC2-6a, d) LC2-6b, e) LC2-4a, f) LC2-4b

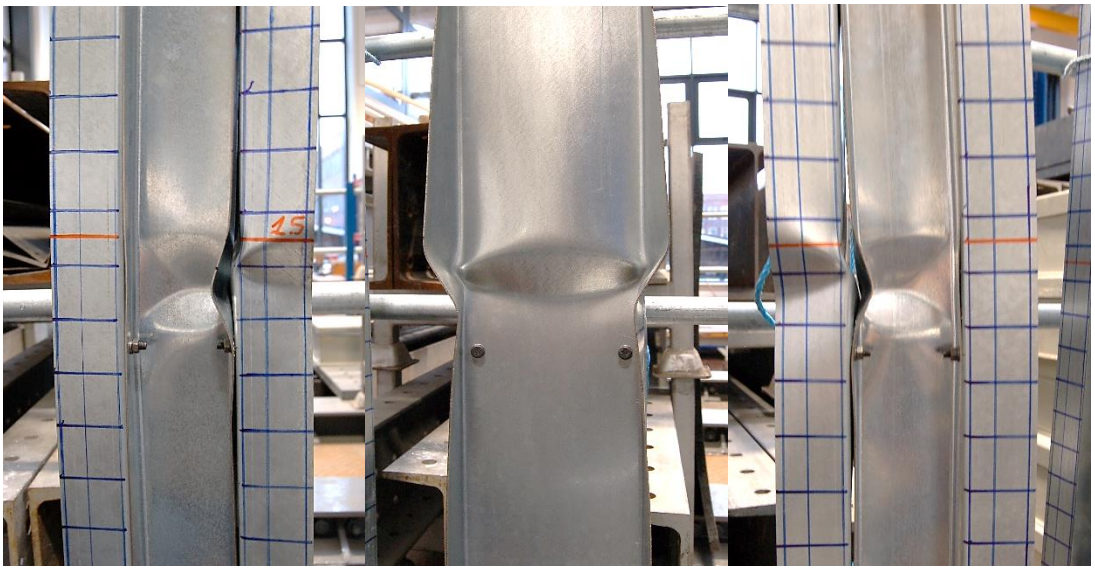

Figure 17: Plastic yield line mechanism in LC2-6b

Figure 18: Failure shape of column LC2-4b

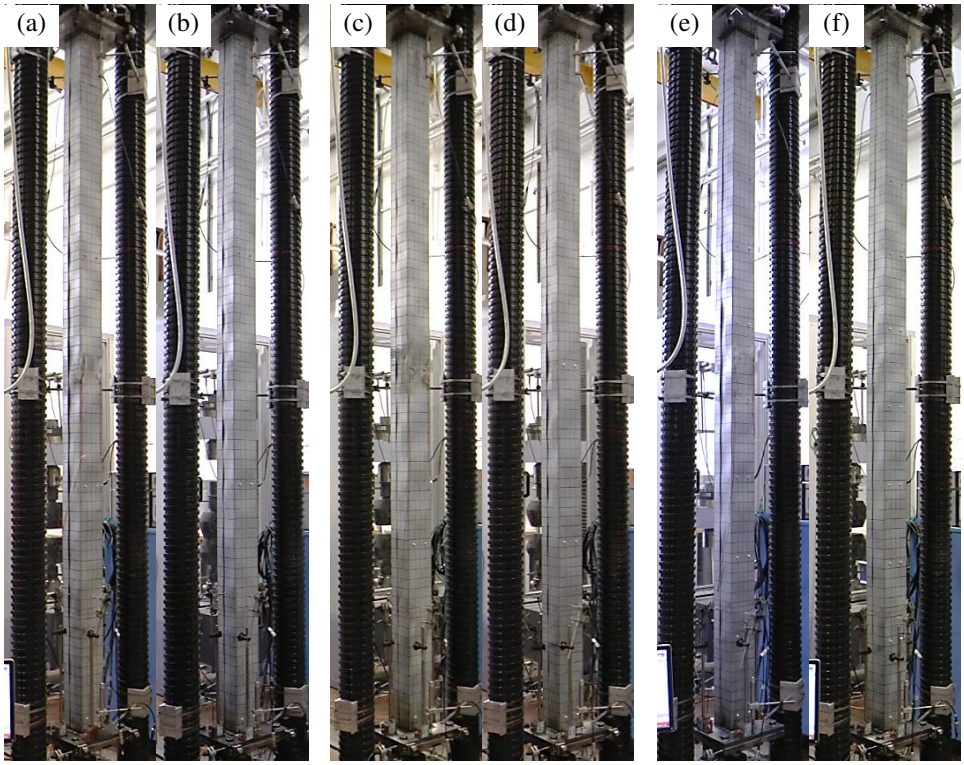

Figure 19: Deformed shape approaching ultimate load in a) LC3-2a, b) LC3-2b, c) LC3-3a, d) LC3-3b, e) LC3-8a, f) LC3-8b

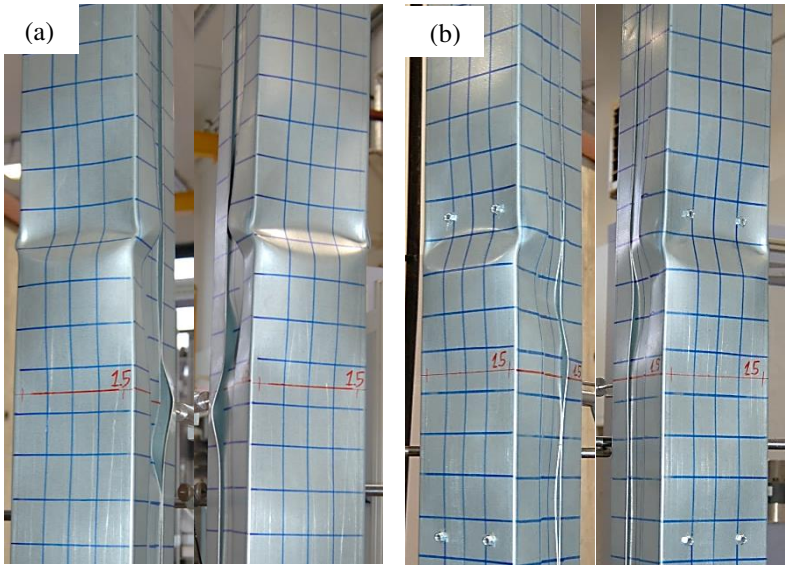

Figure 20: Yield line mechanism in a) LC3-2b, b) LC3-8b

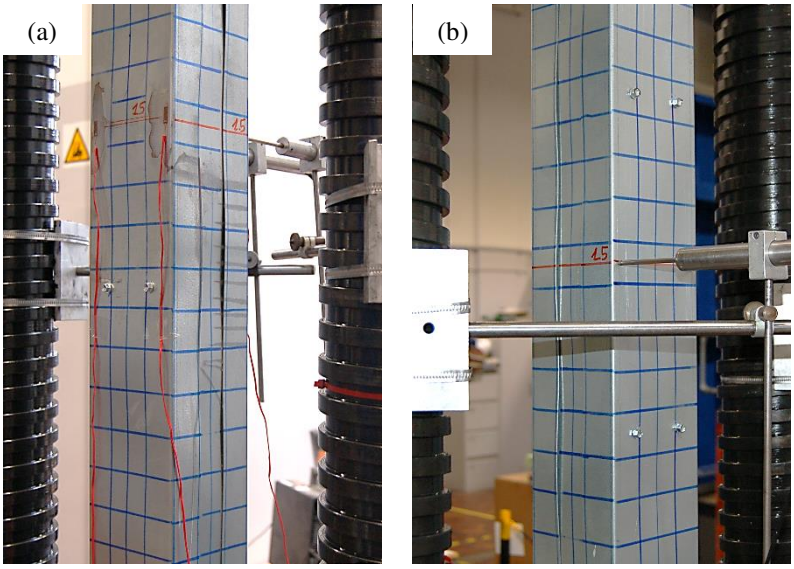

Figure 21: Synchronization between local buckling patterns of lipped and plain channels in a) LC3-8a, b) LC3-8b

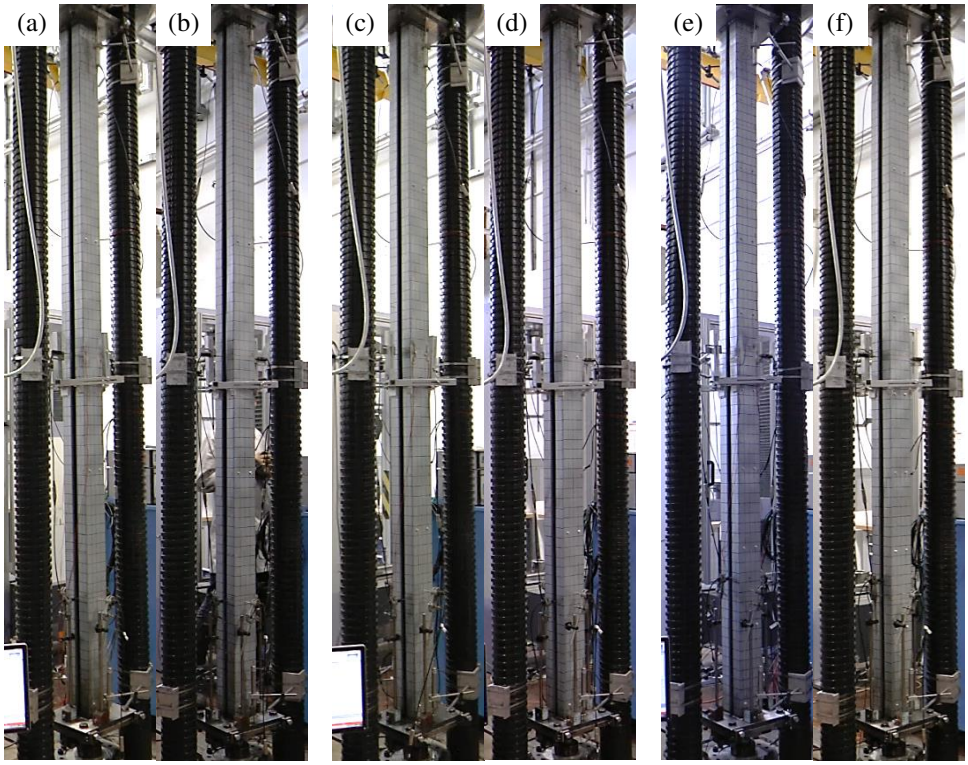

Figure 22: Deformed shape approaching ultimate load in a) LC4-2a, b) LC4-2b, c) LC4-3a, d) LC4-3b, e) LC4-8a, f) LC4-8b

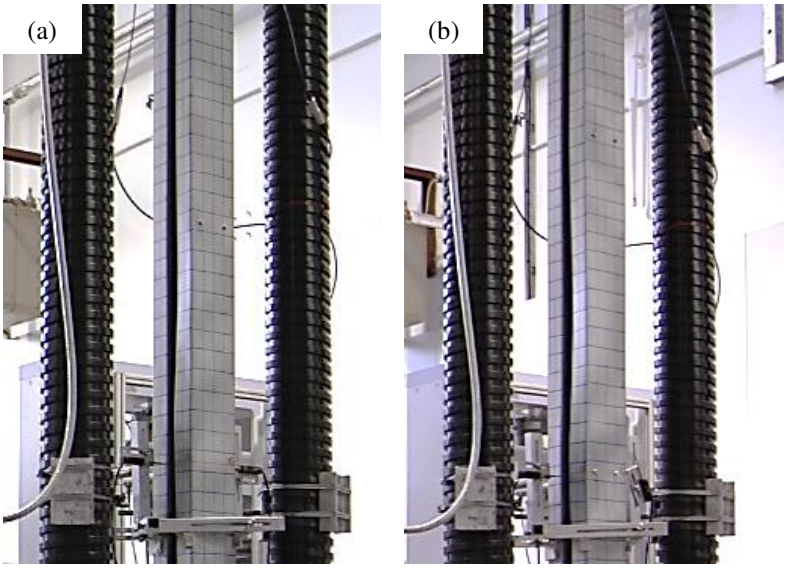

Figure 23: Distortional buckling in lipped channel on compression side in a) LC4-2b, b) LC4-3b

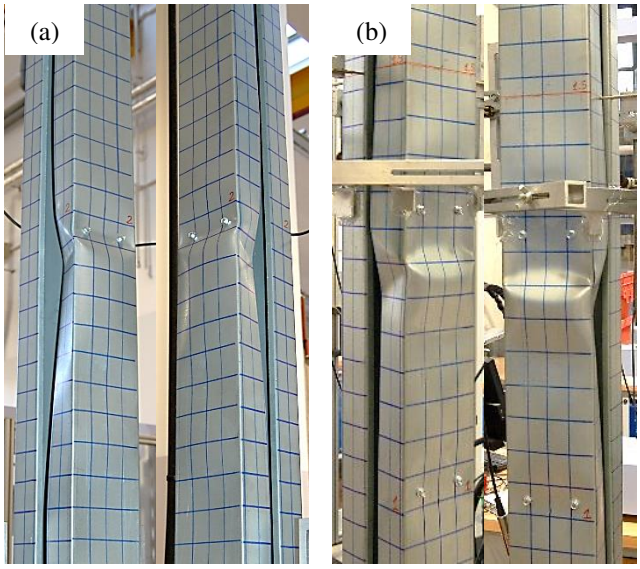

Figure 24: Yield line mechanism in column a) LC4-2b; b) LC4-8b

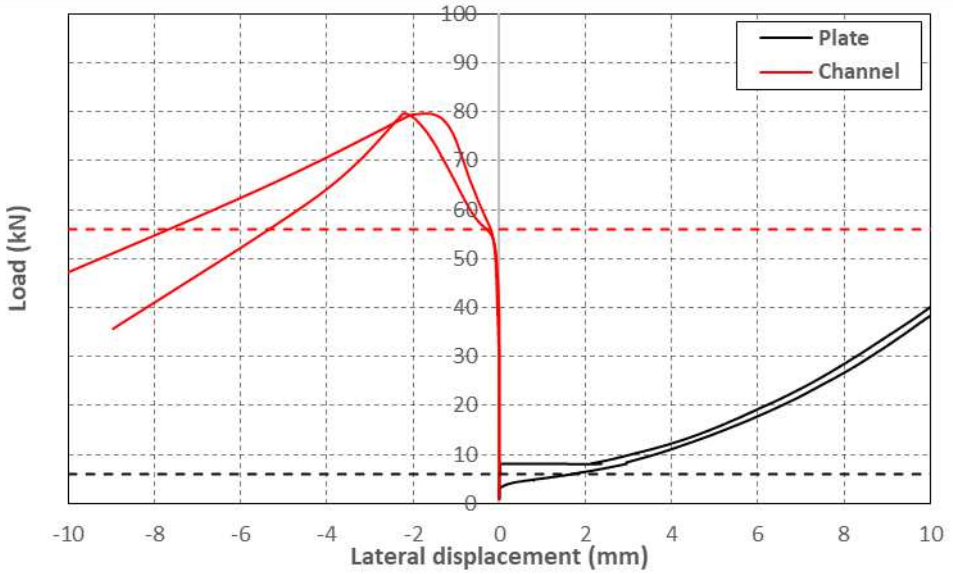

Figure 25: Axial load vs lateral displacements of LC1-2b

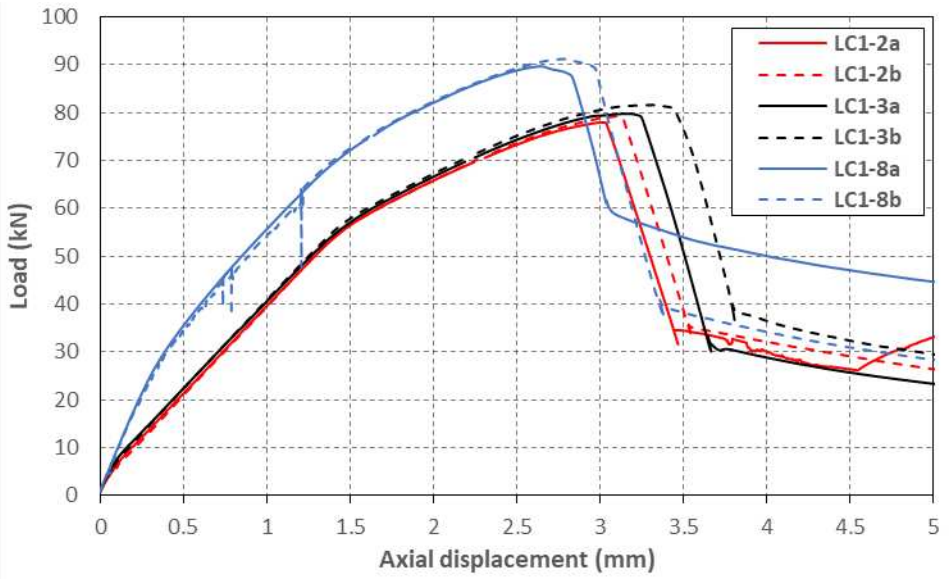

Figure 26: Axial load vs. axial deformation curves: geometry 1

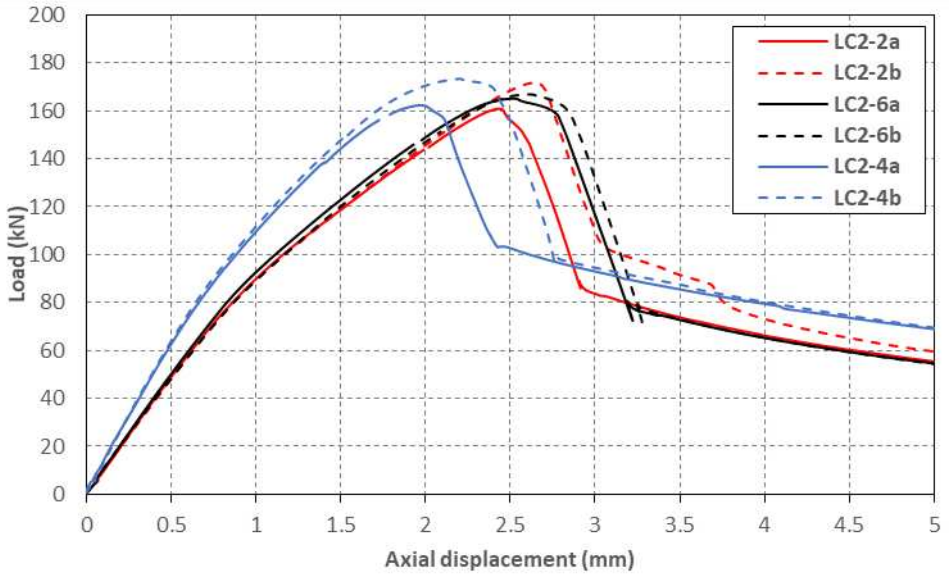

Figure 27: Axial load vs. axial deformation curves: geometry 2

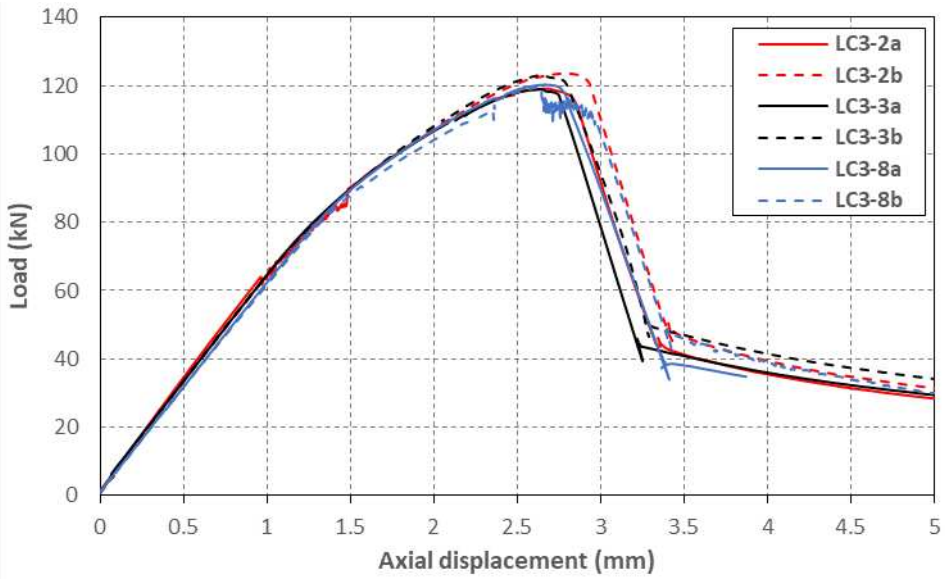

Figure 28: Axial load vs. axial deformation curves: geometry 3

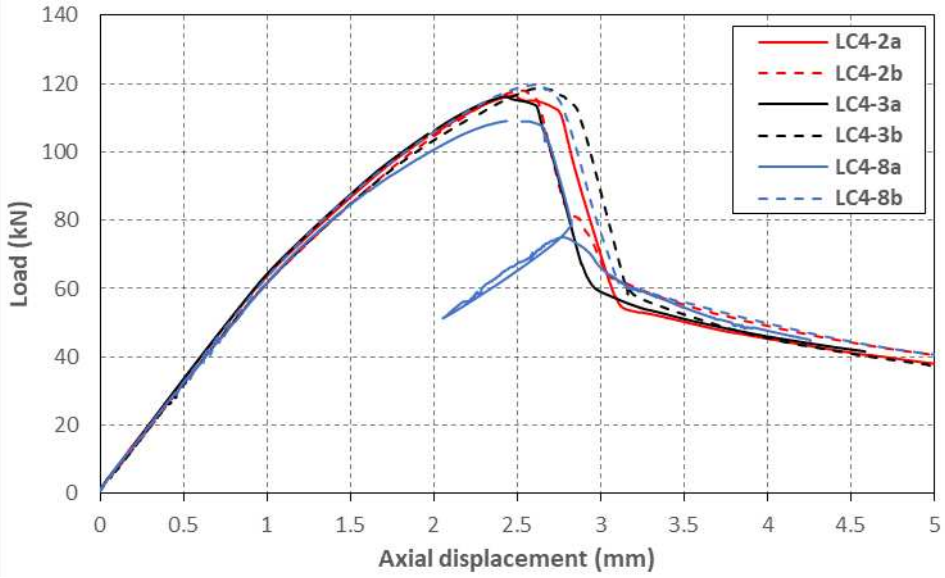

Figure 29: Axial load vs. axial deformation curves: geometry 4